N72-27848

NATIONAL AERONAUTICS AND SPACE ADMINISTRATION
Washington, D. C.

NASA Grant NGL 44-012-006

THE LINEAR POLARIZATION OF LUNAR THERMAL EMISSION AT 3.1 mm WAVELENGTH

Terry L. White

John R. Cogdell

Technical Report No. NGL-006-72-2
April 15, 1972

Submitted by

Electrical Engineering Research Laboratory
The University of Texas at Austin
Austin, Texas

NATIONAL AERONAUTICS AND SPACE ADMINISTRATION
Washington, D. C.

NASA Grant NGL 44-012-006

THE LINEAR POLARIZATION OF LUNAR THERMAL EMISSION AT 3.1 mm WAVELENGTH

Terry L. White

John R. Cogdell

Technical Report No. NGL-006-72-2
April 15, 1972

Submitted by

Electrical Engineering Research Laboratory
The University of Texas at Austin
Austin, Texas

ACKNOWLEDGMENTS

I would like to express my gratitude to my supervising professor, Dr. J. R. Cogdell, for his commitment and support. The other members on my master thesis committee are Dr. A. W. Straiton and Dr. J. N. Douglas.

I wish to thank Mr. Carlos C. Garza and Mr. James W. Johnson for their assistance in taking the data for this thesis.

Thanks are also in order for Mrs. Wanda S. Turner who typed this thesis and Mrs. M. Jean Gehrke who drew the figures.

ABSTRACT

Several observations of the distribution of linearly polarized lunar thermal emission were made at a wavelength of 3.1 mm with The University of Texas 4.88 m parabolic reflector from February to March 1971. A shadow corrected rough surface thermal emission model was least squares fitted to the data. Results indicate an effective lunar dielectric constant of 1.34±.08 with surface roughness characterized by a standard deviation of surface slopes of 18°±2°. A comparison of these results with previously published values at other wavelengths suggests that the effective lunar dielectric constant decreases with decreasing wavelength.

TABLE OF CONTENTS

Page

Abstract iv

List of Figures vi

List of Tables viii

I. Introduction 1

II. Radio Astronomy Concepts 5

III. Smooth Model Derivation 15

IV. Rough Model Derivation 26

V. Beam Smoothing 36

VI. Equipment and Experimental Procedure 46

VII. Data Analysis 51

VIII. Results and Conclusions 59

Appendix A - Derivation of the Brightness Temperature Distribution for a Smooth Dielectric Sphere 78

Appendix B - One Advantage of Displaying Data as a Linear Percent Polarization 85

References 93

LIST OF FIGURES

No.		Page
1	The University of Texas 4.88 Meter Parabolic Reflector	6
2	Two Orthogonal Polarization Positions	7
3	A Typical Radio Telescope System	12
4	Vertical Attenuation Through a Standard Atmosphere	13
5	Reflection and Transmission at a Plane Dielectric Boundary	16
6	Sphere Geometry	20
7	A Frame of Reference for the Observer Showing Polarized Emission	21
8	A Miss of the Apparent Center	23
9	Rough Surface Facet Geometry	28
10	Shadowing Function	33
11	Antenna Pseudo-Polarization for the Quiet Sun (February 9, 1971)	40
12	Antenna Pseudo-Polarization for the Quiet Sun (May 22, 1971)	41
13	Linear Percent Polarization for a Rough Moon	43
14	Linear Percent Polarization Versus Center Offset for $\epsilon = 1.4$ and $\sigma = \tan 20°$	44
15	Receiver Circuit	48
16	One Dimensional Convolution of a Gaussian Antenna Beam with an Approximate Lunar Temperature Distribution	53

17 P1 and P2 Polarizations for Data Set Number 1 62

18 Linear Percent Polarization for Data Set Number 1 63

19 P1 and P2 Polarizations for Data Set Number 2 64

20 Linear Percent Polarization for Data Set Number 2 65

21 P1 and P2 Polarizations for Data Set Number 3 66

22 Linear Percent Polarization for Data Set Number 3 67

23 P1 and P2 Polarizations for Data Set Number 4 68

24 Linear Percent Polarization for Data Set Number 4 69

25 P1 and P2 Polarizations for Data Set Number 5 70

26 Linear Percent Polarization for Data Set Number 5 71

27 P1 and P2 Polarizations for Data Set Number 6 72

28 Linear Percent Polarization for Data Set Number 6 73

29 Comparison of Results 76

LIST OF TABLES

No.		Page
1	Lunar Observations	49
2	Experimental Results	60

I. INTRODUCTION

Measurements of the linear polarization of lunar thermal emission were conducted at a wavelength of 3.1 mm with the high resolution (0.045° HPBW) 4.88 meter parabolic reflector at The University of Texas Millimeter Wave Observatory. The best overall least squares fit to the entire data implies an effective lunar dielectric constant of 1.34±.08, and a standard deviation for lunar slopes of 18°±2°. A comparison of these results with those of previous studies indicates that the effective lunar dielectric constant decreases with decreasing wavelength of observation. Indications are the lunar surface is rough on a scale of a few millimeters. There is a need to accurately measure the linear polarization of lunar thermal emission at several wavelengths to clearly define a wavelength dependence of the effective dielectric constant.

At optical wavelengths lunar radiation is primarily reflected solar radiation, while at radio wavelengths lunar radiation is due to thermal emission. The subsurface lunar radiation strikes the surface and is polarized, as described by Fresnel's equations, into two orthogonal components. This emission process is further modified by the presence of surface roughness and shadowing.

It is possible to observe the distribution of the percent polarization across the lunar disk with high resolution (narrow beamwidth) antennas.

From this distribution, values for the effective dielectric constant and surface slopes can be obtained.

Troitsky[1] (1954) first postulated that ϵ, the relative lunar dielectric constant, could be obtained from the distribution of excess polarization across the lunar disk. He neglected surface roughness as unimportant in practice.

Soboleva[2] (1962) was one of the first experimenters to observe the excess lunar polarization. She found $\epsilon = 1.65$ at a wavelength λ of 3.2 cm, with a rough surface model characterized by a uniform distribution of surface normals in a 20° cone.

Baars, et al.[3] (1963) found $\epsilon = 1.5$ at $\lambda = 2.07$ cm with a 15° cone rough model. They were the first experimenters to suggest that ϵ decreases with decreasing wavelength of observation.

Heiles and Drake[4] (1963) found $\epsilon = 2.1 \pm 0.3$ at $\lambda = 21$ cm and they concluded that a smooth model gave the best fit to their experimental data. This suggested that the Moon was relatively smooth on a 21 cm scale.

Golnev and Soboleva[5] (1964) found $\epsilon = 2.0$ (estimated from their published data) at $\lambda = 6.3$ cm with a 20° cone rough model.

Moran[6] (1965) at $\lambda = 8.5$ mm found $\epsilon = 1.7$ with roughness characterized by tilted facets with a 15° standard deviation for his normal probability density of lunar slopes.

Hagfors[7] (1965) tried to reconcile the large values for the dielectric constants obtained by radar techniques with the smaller dielectric constants obtained by lunar emission measurements. He also proposed a two layered lunar dielectric surface[8] to account for the wavelength dependence of the effective dielectric constant.

Losovskii[9] (1966) found $\epsilon = 1.5 \pm 0.2$ with roughness of 15°±10° at $\lambda = 8$ mm. He was the first worker to approximately account for intermediate scale surface roughness by correcting his model using radar results[10] as a guide. This correction increased his effective dielectric constant to $2.3 \pm .5$.

Davies and Gardner[11] (1966) measured $\epsilon = 2.2 \pm 0.1$ at $\lambda = 6$ cm, $\epsilon = 2.25 \pm 0.05$ at $\lambda = 11$ cm, and $\epsilon = 2.5 \pm 0.15$ at $\lambda = 21$ cm. Roughness was characterized by a 8°-16° scatter of slopes.

Clegg and Carter[12] (1970) measured $\epsilon = 3.0 \pm 0.3$ at $\lambda = 1.2$ mm, the smallest wavelength of observation to date.

This study was motivated by the desire to obtain the dielectric constant and surface roughness of the Moon at the shorter millimeter wavelengths. Shadowing due to surface roughness has been crudely approximated or completely neglected in the past. This study takes shadowing into account by employing a probabilistic shadowing function.

In Chapter II the reader is introduced to such radio astronomy concepts as polarization, beam smoothing, receiver noise and atmospheric attenuation.

In Chapter III the refraction of a plane wave incident on a plane dielectric boundary is described. A smooth lunar thermal emission model is then derived.

In Chapter IV the smooth model is modified to account for large scale surface roughness. The important effect of shadowing is examined.

In Chapter V the antenna response to the rough model is derived. Beam ellipiticity is experimentally verified.

In Chapter VI the equipment used in the present study and the data taking procedure are briefly described.

In Chapter VII the data analysis scheme is explained. Appropriate numerical techniques are discussed.

In Chapter VIII the results and conclusions of this study are stated. All possible sources of error are summarized. The experimental results are compared with those of previous studies.

II. RADIO ASTRONOMY CONCEPTS

In this chapter several radio astronomy concepts are presented in order to form a basis for understanding material in later chapters.

Many different types of radio telescopes are in existence today, however for brevity, only parabolic reflector antennas will be considered since this type of antenna is used by The University of Texas Millimeter Wave Observatory.

The parabolic reflector concentrates incoming radiation at a rectangular waveguide feed located at the focus of the reflector as pictured in Fig. 1. The rectangular feed is operated in the TE_{10} (dominant) mode, and as a consequence, the polarization of the electric field is fixed perpendicular to the long dimension of the rectangular feed aperture. This implies that the feed, and therefore the entire antenna, will only receive radiation with electric field components parallel to the feed polarization (components perpendicular to the feed polarization are not received). The plane of polarization for the entire antenna may be rotated 90 electrical degrees by simply rotating the feed a corresponding amount. In Fig. 2 a set of orthogonal polarization positions are defined as viewed by an observed source. The P1 position corresponds to the alignment of the feed polarization along the y (declination) axis while the P2 position corresponds to the alignment of the feed polarization along the x (hour angle) axis.

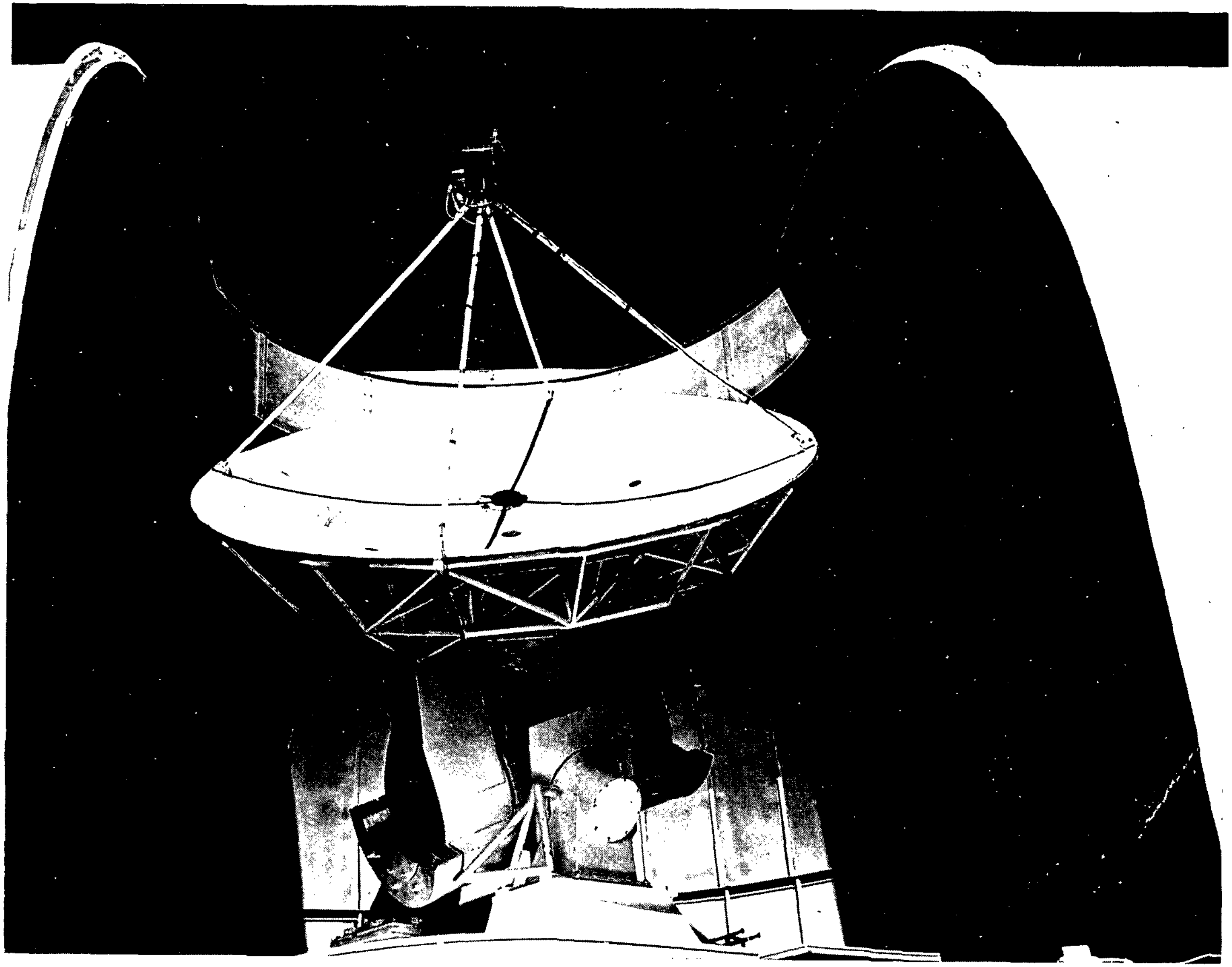

THE UNIVERSITY OF TEXAS 4.88 METER PARABOLIC REFLECTOR

Fig. 1

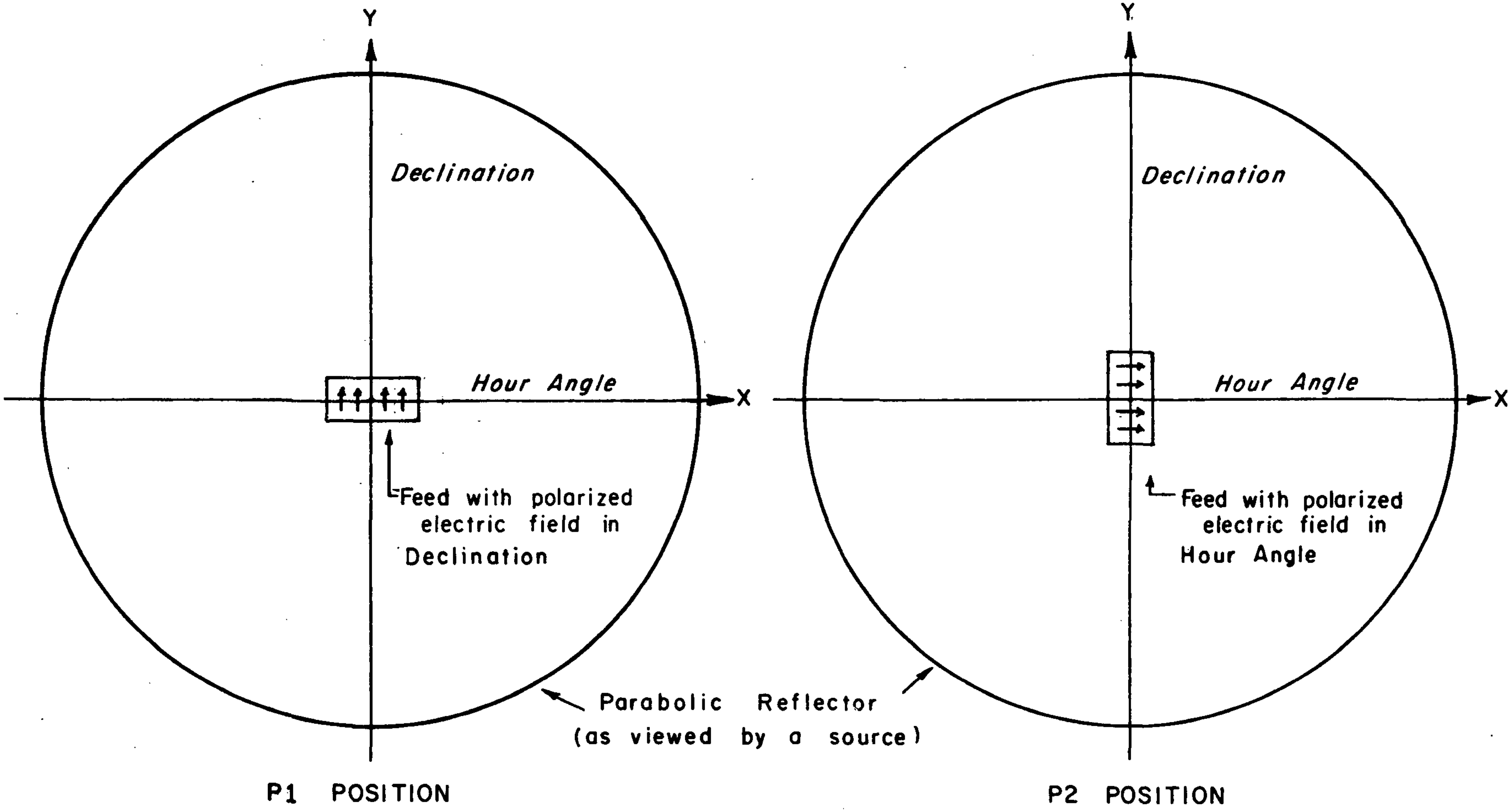

TWO ORTHOGONAL POLARIZATION POSITIONS

Fig. 2

An equatorial mount for the antenna shown in Fig. 1 is the most convenient type of antenna mount for radio astronomy work. The polar axis of the mount is aligned parallel to the Earth's axis of rotation, and the declination axis is aligned perpendicular to the polar axis. In the equatorial system, the position coordinates are hour angle and declination. The advantage of using an equatorial mount is the fact that radio sources move in hour angle at a more or less constant rate but remain relatively fixed in declination. Thus only motion in hour angle is required to track sources.

Radio sources emit radiation in the form of plane waves which are in general partially polarized, that is, there are two components, one part completely polarized and the other part completely unpolarized.

The polarization of a plane wave is described by the orientation of the resultant electric field vector in the plane of constant phase (normal to the direction of propagation) for the plane wave. Generally a completely polarized plane wave will be elliptically polarized and the tip of its electric field vector will trace out an ellipse in the plane of constant phase.

Special types of polarization are linear and circular where the tip of the resultant electric field vector traces out a fixed line and a circle, respectively, in the plane of constant phase for the wave.

A completely unpolarized plane wave consists of a superposition of a large number of statistically independent waves of a variety of polarizations. The wave has no preferential polarization and the resultant electric field vector traces out a random pattern in the plane of constant phase for the wave. The time averaged Poynting vectors measured in any two orthogonal polarizations are always equal for a wave of this type. Thermal blackbody radiation is a prime example of completely unpolarized radiation.

A fundamental equation of radio astronomy that relates the measured power at the terminals of the antenna to the brightness of a completely unpolarized source being observed is

$$w(\varphi', \theta') = \tfrac{1}{2}A_e \iint_{\text{source}} B(\varphi, \theta)\, P_n(\varphi-\varphi', \theta-\theta')\, d\Omega, \tag{1}$$

where $w(\varphi', \theta')$ is the measured power in watts-Hz^{-1} as a function of angular coordinates φ' and θ'. The brightness of the source is $B(\varphi, \theta)$ in watts-m^{-2}-Hz^{-1}-rad^{-2} as a function of angular coordinates φ and θ. The normalized antenna power radiation pattern is $P_n(\varphi, \theta)$ and A_e is the effective area of the antenna in m^2. The factor of $\frac{1}{2}$ is inserted because the antenna can only respond to one half of the incident radiation from the unpolarized source. Also note that

$$d\Omega = \sin\theta \, d\theta \, d\varphi. \tag{2}$$

At radio wavelengths the Moon acts as a source of thermal radiation so that Equation 1 can be modified to express measured temperature in one linear polarization at the antenna terminals in terms of the source brightness temperature. The modified equation is

$$T_a(\varphi', \theta') = \frac{1}{\Omega_a} \iint_{\text{source}} T_s(\varphi, \theta)\, P_n(\varphi-\varphi', \theta-\theta')\, d\Omega, \tag{3}$$

where $T_a(\varphi', \theta')$ is the antenna temperature in °K and $T_s(\varphi, \theta)$ is the source brightness temperature in °K. Equation 3 states that, in angle space, the antenna temperature is similar to the convolution of the source brightness temperature distribution and the normalized antenna pattern, the entire convolution being normalized by the antenna solid angle. An analogous situation is the transient convolution encountered in circuit theory, where P_n corresponds to the impulse response of the system transfer function, and T_s and T_a are similar to the signal input and signal output, respectively. The angle domain is also analogous to the time domain and the antenna beam solid angle in rad^2 is

$$\Omega_a = \iint_{\text{sky}} P_n(\varphi, \theta)\, d\Omega. \tag{4}$$

A useful concept in radio astronomy is the minimum amount of detectable receiver output appearing on the chart record. Because all receivers have some finite amount of noise present, the minimum detectable signal is approximately the root mean square (rms) of the receiver output in the absence of signal, which is given by:

$$\Delta T_{rms} = \frac{K_r\, T_{sys}}{\sqrt{\Delta\nu n\tau}}, \tag{5}$$

where T_{sys} is the system noise temperature in °K; K_r is a dimensionless constant (approximately 2) which depends upon the type of receiver used; $\Delta\nu$ is the predetection noise bandwidth of the receiver in $\sec^{-1}$; τ is the postdetection integration time in sec and n is the number of records averaged.

It is common practice to quote a ΔT_{rms} based on a one second integration time. To find the ΔT_{rms} for a set of data where averaging records are used to decrease the noise,

$$\Delta T_{rms} = \frac{\Delta T_{rms}\big|_{\tau=1\ \text{sec}}}{\sqrt{n\tau}} \ . \qquad (6)$$

A schematic representation of a typical radio telescope system is shown in Fig. 3. The system noise temperature is

$$T_{sys} = T_a + T_\ell \left[\frac{1}{e} - 1\right] + T_r \left(\frac{1}{e}\right), \qquad (7)$$

where T_ℓ is the physical temperature of the transmission line between the antenna and receiver in °K; T_r is the receiver noise temperature referred to its input in °K, and T_a is defined the same as in Equation 1. Also, e is the dimensionless transmission line power efficiency.

Atmospheric attenuation of electromagnetic radiation at millimeter wavelengths is primarily due to molecular resonances of the oxygen molecule and absorption caused by water vapor. Since these sources of attenuation vary with the frequency of millimeter radiation, several regions of minimum attenuation or "windows" are formed. Fig. 4 shows the one-way transmission vertically through a standard atmosphere (7.5 gm/cc of water vapor) after Straiton and Fannin[13]. The total

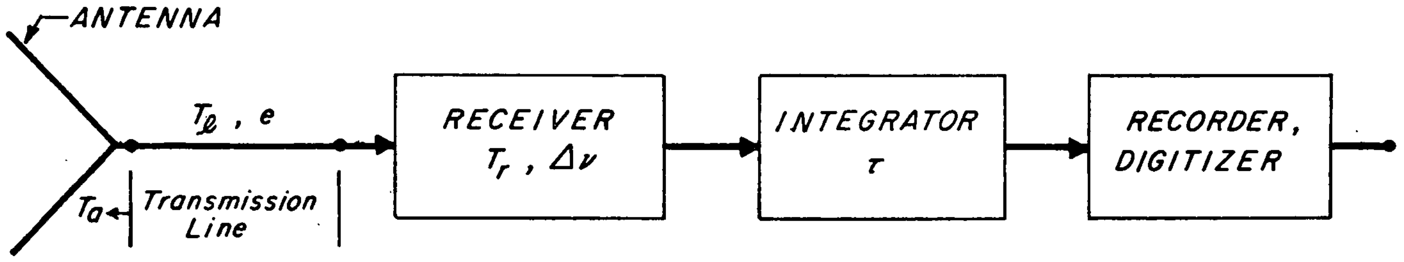

A TYPICAL RADIO TELESCOPE SYSTEM

Fig. 3

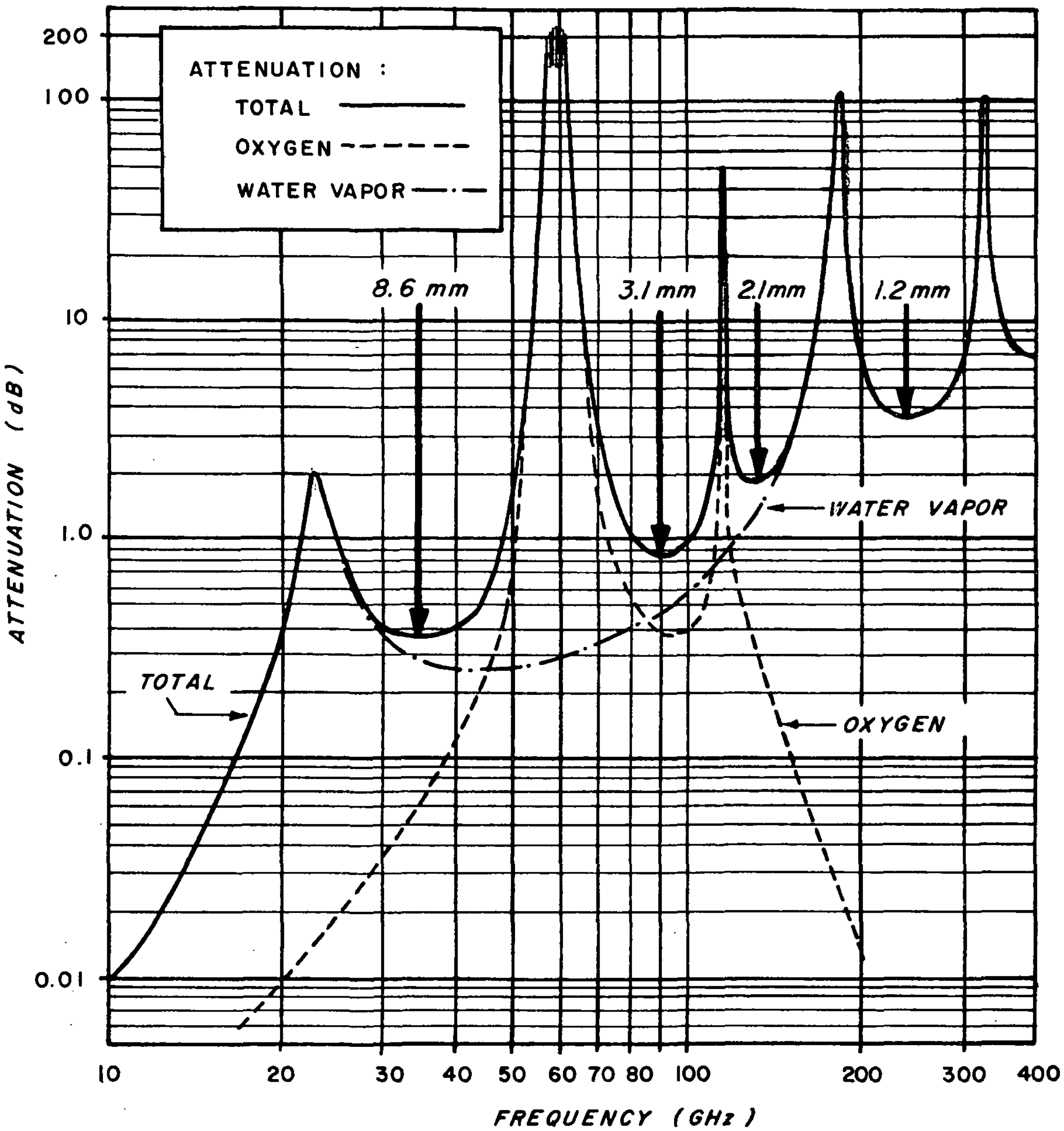

VERTICAL ATTENUATION THROUGH A STANDARD ATMOSPHERE

Fig. 4

attenuation in dB is the sum of oxygen and water vapor attenuations. The various windows are located at approximately 1.2, 2.1, 3.1 and 8.6 millimeters wavelength.

III. SMOOTH MODEL DERIVATION

This chapter is devoted to the derivation of an emission model for a smooth dielectric sphere scaled to approximate the Moon as observed from Earth. Suppose an electromagnetic plane wave strikes a plane dielectric boundary at an angle of incidence β_i, as shown in Fig. 5. The angle β_i is measured between the surface normal $\vec{n}$ and the plane wave propagation vector $\vec{k}_i$. The two media are assumed to be homogeneous, isotropic, and semi infinite in extent. A plane of incidence is defined as the plane containing the surface normal $\vec{n}$ and the unit normal to the incident plane wave $\vec{k}_i$. In Fig. 5 the plane of incidence coincides with the page. The incident plane wave can always be resolved into a component parallel to the plane of incidence and a component perpendicular to the plane of incidence. The subscripts "i", "r", and "t" refer to incident, reflected, and transmitted quantities, respectively. The circle notation implies a direction normal to the plane of incidence, out of the page, and the dot notation implies an opposite direction.

Assume medium 2 has a relative permeability μ of unity and a relative permittivity of ϵ (hereafter referred to as the dielectric constant) and also assume medium 1 is free space, or:

$$\begin{aligned} \epsilon_2 &= \epsilon\epsilon_o & \epsilon_1 &= \epsilon_o \\ \mu_2 &= \mu_o & \mu_1 &= \mu_o \\ \sigma_2 &\approx 0 & \sigma_1 &= 0 \end{aligned} \tag{8}$$

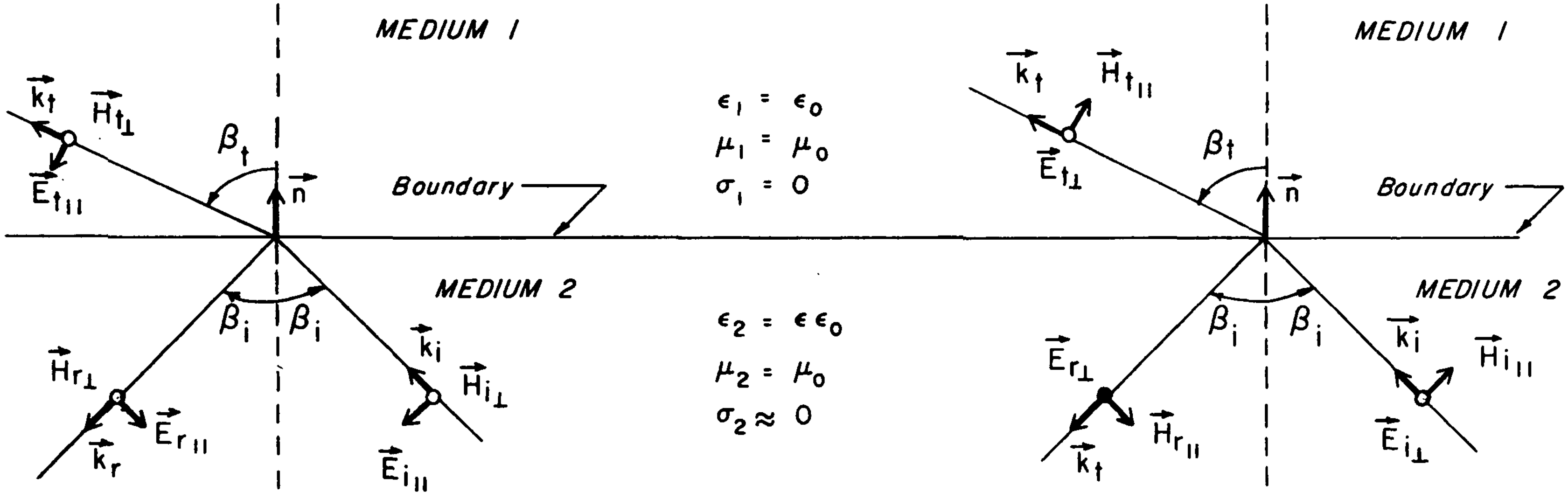

POLARIZATION PARALLEL TO THE PLANE
OF INCIDENCE

POLARIZATION PERPENDICULAR TO THE PLANE
OF INCIDENCE

REFLECTION AND TRANSMISSION AT A PLANE DIELECTRIC BOUNDARY

Fig. 5

According to Stratton[14], the Fresnel formulas for the ratios of transmitted energy to incident energy in planes parallel and perpendicular to the plane of incidence are

$$\tau_{\parallel}(\beta_i, \beta_t) = \frac{\sin 2\beta_i \sin 2\beta_t}{\sin^2 (\beta_i + \beta_t) \cos^2 (\beta_i - \beta_t)} , \tag{9}$$

and

$$\tau_{\perp}(\beta_i, \beta_t) = \frac{\sin 2\beta_i \sin 2\beta_t}{\sin^2 (\beta_i + \beta_t)} , \tag{10}$$

where β_t is the angle of transmission measured from $\vec{n}$ to $\vec{k}_t$. Snell's Law states that

$$\sin \beta_i = \frac{1}{\sqrt{\epsilon}} \sin \beta_t, \tag{11}$$

or

$$\cos \beta_i = \sqrt{1 - \frac{1}{\epsilon} \sin^2 \beta_t} . \tag{12}$$

Dropping the "t" subscript and substituting Equations 11 and 12 into 9 and 10 we have

$$\tau_{\parallel}(\epsilon, \beta) = \frac{4\epsilon \cos \beta \sqrt{\epsilon - \sin^2 \beta}}{\left[\epsilon \cos \beta + \sqrt{\epsilon - \sin^2 \beta}\right]^2} , \tag{13}$$

and

$$\tau_{\perp}(\epsilon, \beta) = \frac{4 \cos \beta \sqrt{\epsilon - \sin^2 \beta}}{\left[\cos \beta + \sqrt{\epsilon - \sin^2 \beta}\right]^2} . \tag{14}$$

Suppose that the indicent energy in medium 2 is due to the thermal emission of that medium. This would imply that the incident energy is completely unpolarized or, taken another way, that the time averaged Poynting vector measured in any two orthogonal polarization directions in medium 2 are equal. Since there is no preferential polarization of energy in medium 2, the time averaged magnitudes of the transmitted energy in medium 1 will depend only upon the magnitudes of $\tau_{\parallel}(\epsilon, \beta)$ and $\tau_{\perp}(\epsilon, \beta)$.

Actually, the mechanism of thermal emission in medium 2 is described by a superposition of an infinite number of plane waves at an infinite number of wavelengths propagating in an infinite number of directions in medium 2. There is, however, only one unique direction in medium 2, namely $\vec{k}_t$, that will allow transmitted plane waves to be observed at a direction $\vec{k}_t$. Also, observations are taken in such a way as to filter out all radiation except for a narrow band about λ, the wavelength of interest. Therefore only one plane wave propagating in the $\vec{k}_i$ direction in a narrow band about λ is observed out of many such plane waves.

Now suppose that a smooth, very slightly lossy, homogeneous dielectric sphere with dielectric constant ϵ were located in free space. Assume for now that the sphere possesses some surface temperature distribution $T(\theta, \beta)$. Since the sphere is slightly lossy, the thermal radiation emitted from the sphere at millimeter wavelengths originates at some depth beneath the surface.

The sphere has a radius R equal to the mean radius of the Moon, and the sphere is located at distance D from an observer equal to the mean Earth-Moon separation. The sphere now approximates a smooth, uniformly heated Moon. Since $R >> \lambda$ the curvature of the surface approaches a flat plane. Equations 13 and 14 will now be valid for a point on the surface of the sphere. Fig. 6 shows the geometrical configuration for an observer at a distance D from the sphere. Note that

$$\beta = \delta + \rho, \tag{15}$$

where β is the angle between the surface normal and the observer's line-of-sight; δ is the position angle of point P with respect to the observer measured at point C, and ρ is the difference between β and δ. In the case of the Moon as seen from the Earth the angle ρ is small and

$$\sin \rho \approx \rho, \tag{16}$$

so that

$$\beta = \sin^{-1} (r_t/R) + \sin^{-1}\left[\frac{r_t/R}{\sqrt{(D/R)^2 - 2(D/R)\sqrt{1 - (r_t/R)^2} + 1}}\right], \tag{17}$$

where r_t is the measured from the apparent center of the disk to the point of emission.

In Fig. 7 a frame of reference for the observer is shown using a polar coordinate system. $E_{t_\parallel}$ and $E_{t_\perp}$ are the transmitted electric fields, and θ is the position angle of the point P while θ_o is the position

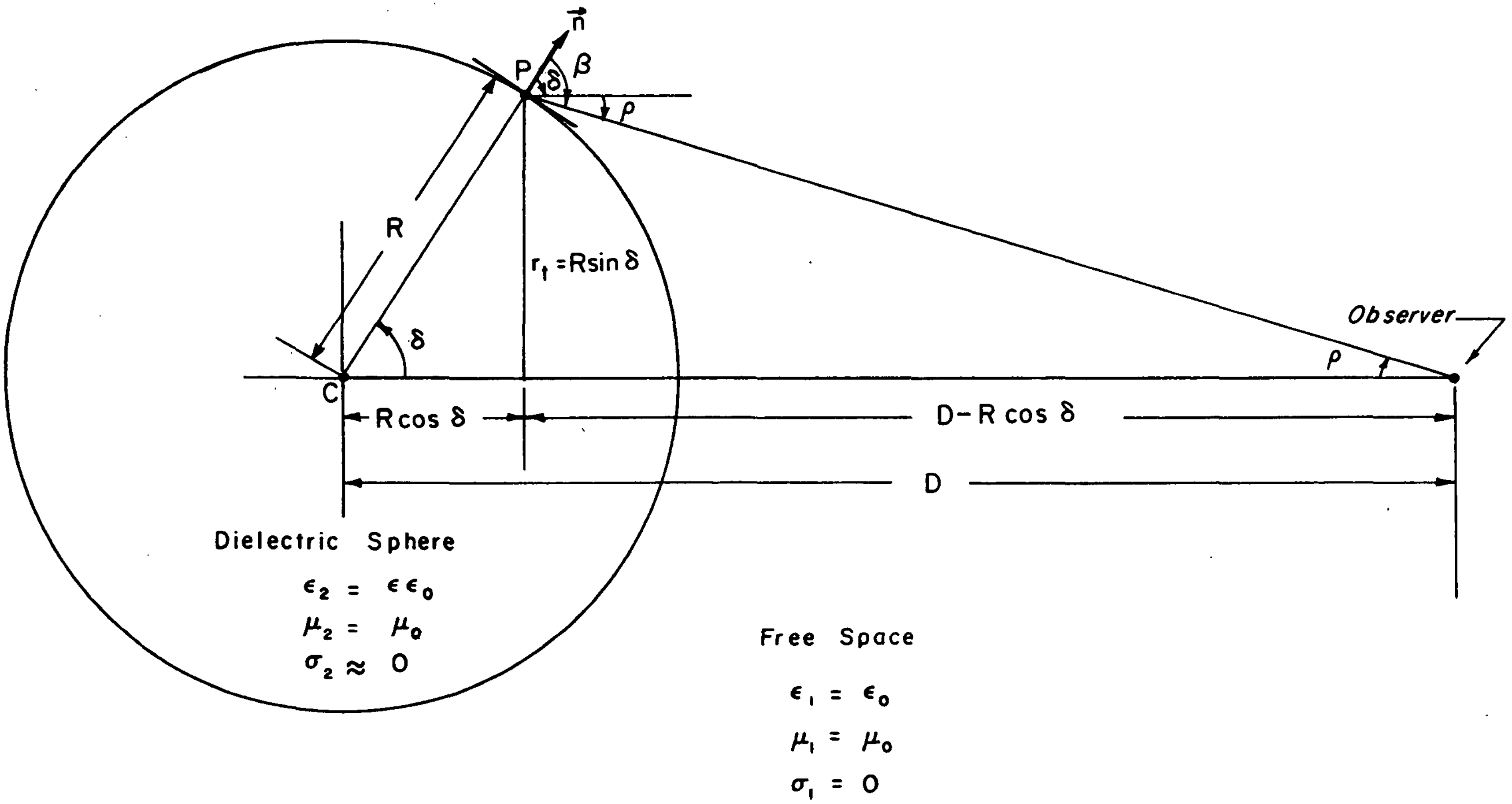

SPHERE GEOMETRY

Fig. 6

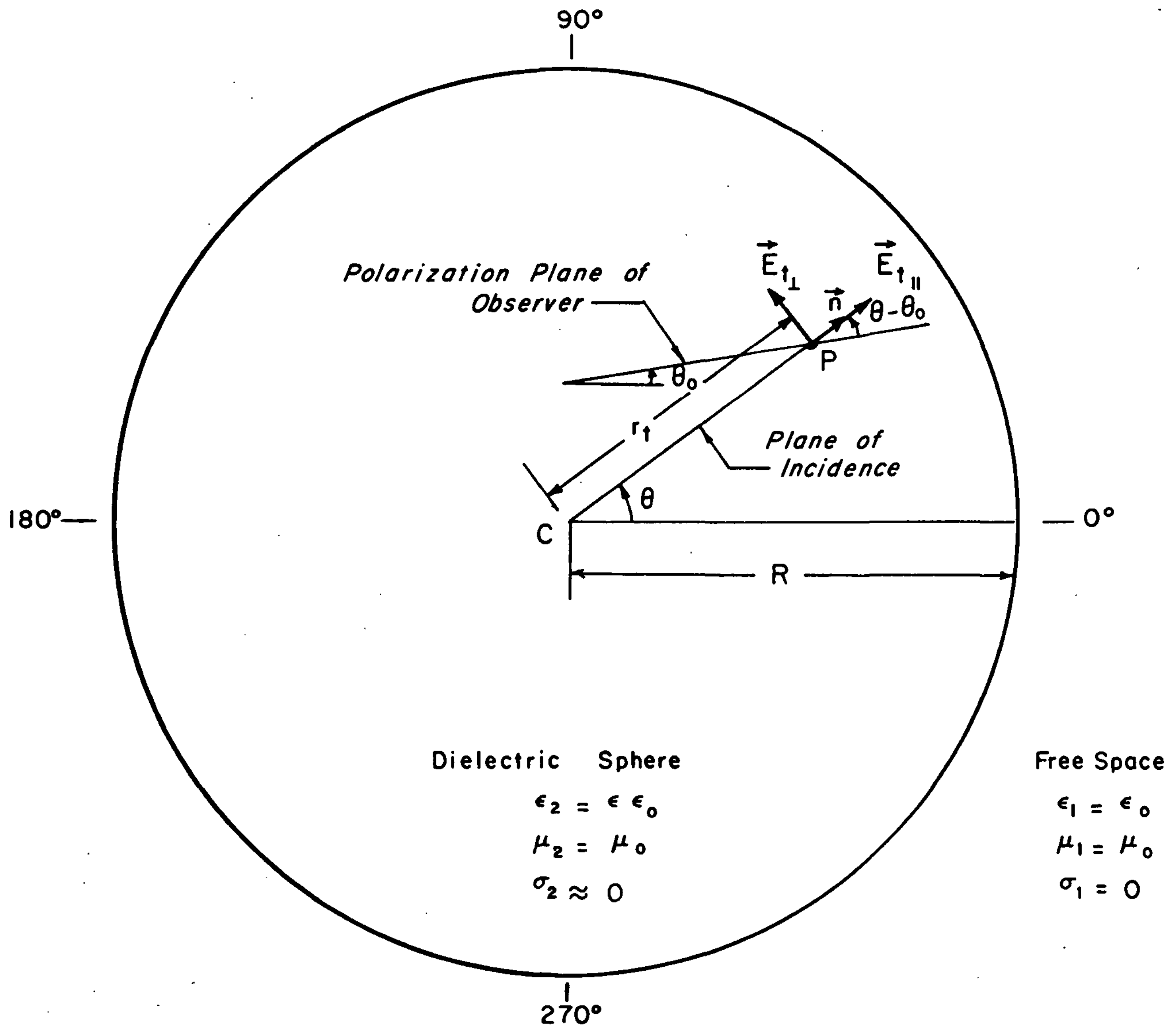

A FRAME OF REFERENCE FOR THE OBSERVER SHOWING POLARIZED EMISSION

Fig. 7

angle of the observer's plane and polarization. Both angles are measured counterclockwise from a reference line taken to be the equator of the sphere. The plane of incidence always lies along any radius drawn from point C to point P. The received radiation from point P at a temperature T as derived from Appendix A is,

$$T_{P1}(\epsilon, \beta, \theta) = T[\tau_{\parallel}(\epsilon, \beta) \sin^2 \theta + \tau_{\perp}(\epsilon, \beta) \cos^2 \theta], \tag{18}$$

and

$$T_{P2}(\epsilon, \beta, \theta) = T[\tau_{\parallel}(\epsilon, \beta) \cos^2 \theta + \tau_{\perp}(\epsilon, \beta) \sin^2 \theta], \tag{19}$$

where $\theta_o = 0°$ by convention, also $P1 \hat{=} \theta_o + 90°$; $P2 \hat{=} \theta_o$. Equations 18 and 19 are measureable quantities for an antenna with an infinitely narrow beamwidth. Note that θ now becomes the angle between the plane of incidence and the observer's plane of polarization.

For a scan of the sphere across the apparent equator ($\theta = 0°$),

$$T_{P1}(\epsilon, \beta, 0°) = T(\beta, 0°) \quad \tau_{\perp}(\epsilon, \beta), \tag{20}$$

and

$$T_{P2}(\epsilon, \beta, 0°) = T(\beta, 0°) \quad \tau_{\parallel}(\epsilon, \beta), \tag{21}$$

where $T(\beta, 0°)$ is the brightness temperature distribution across the apparent equator of the lunar disk.

It is possible now to probe the functions $\tau_{\parallel}(\epsilon, \beta)$ and $\tau_{\perp}(\epsilon, \beta)$ independent of each other. In practice, however, the antenna beam can miss the apparent center by some small distance d as shown in Fig. 8.

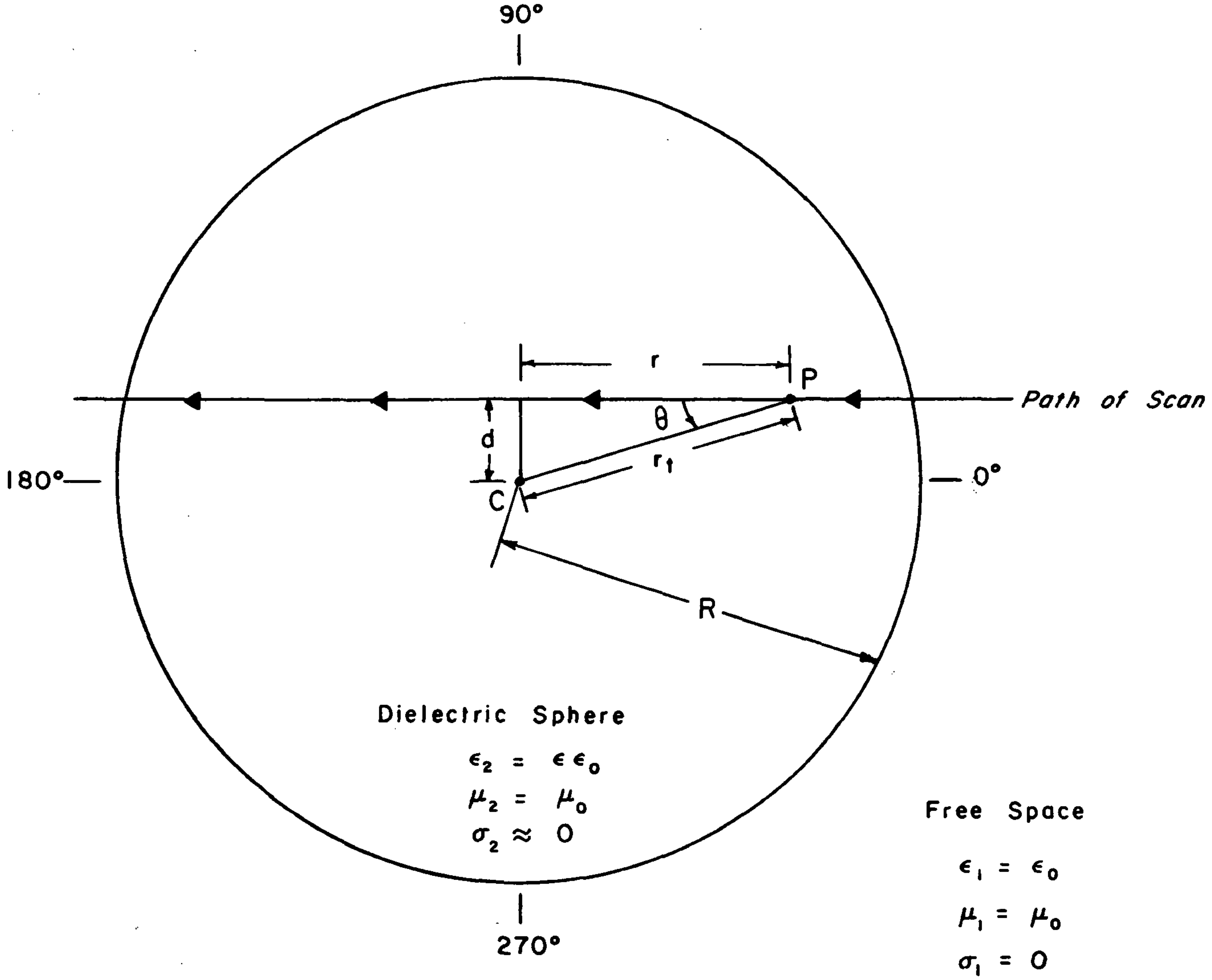

A MISS OF THE APPARENT CENTER

Fig. 8

Then

$$r_t = \sqrt{r^2 + d^2}, \tag{22}$$

and

$$\theta = \sin^{-1}\left(\frac{d}{r_t}\right), \tag{23}$$

where r_t is the true distance from point P and point C. Using Equations 17, 22, and 23, Equations 18 and 19 can be rewritten as

$$T_{P1}(\epsilon, r, d) = T(\beta, \theta)\left[\tau_{\parallel}(\epsilon, r, d)\left(\frac{d^2}{r^2 + d^2}\right) + \tau_{\perp}(\epsilon, r, d)\left(\frac{r^2}{r^2 + d^2}\right)\right], \tag{24}$$

and

$$T_{P2}(\epsilon, r, d) = T(\beta, \theta)\left[\tau_{\parallel}(\epsilon, r, d)\left(\frac{r^2}{r^2 + d^2}\right) + \tau_{\perp}(\epsilon, r, d)\left(\frac{d^2}{r^2 + d^2}\right)\right], \tag{25}$$

where $T(\beta, \theta)$ is the true surface temperature distribution of the Moon.

The percent polarization is now defined as

$$\%\mathrm{Pol}(\epsilon, r, d) \triangleq \frac{T_{P2}(\epsilon, r, d) - T_{P1}(\epsilon, r, d)}{T_{P2}(\epsilon, r, d) + T_{P1}(\epsilon, r, d)}, \tag{26}$$

or

$$\%\mathrm{Pol}(\epsilon, r, d) = \frac{\tau_{\parallel}(\epsilon, r, d) - \tau_{\perp}(\epsilon, r, d)}{\tau_{\parallel}(\epsilon, r, d) + \tau_{\perp}(\epsilon, r, d)}\left(\frac{r^2 - d^2}{r^2 + d^2}\right). \tag{27}$$

This model now predicts the noise free, linear percent polarization for a smooth, homogeneous Moon (for an infinitely narrow beamwidth antenna). Since $T(\beta, \theta)$ cancels out of the percent polarization, the model is independent of the temperature variations across the lunar surface.

On a scale of a few millimeters, however, the Moon is not very smooth and one would expect that the smooth model would incorrectly estimate the percent polarization. Accordingly, the derivation of a rough lunar model with shadowing follows in Chapter IV.

IV. ROUGH MODEL DERIVATION

Surface roughness on the Moon may be classified into three separate regimes. The first regime consists of a slowly undulating, smooth surface that is a plane in the mean. The undulations are much greater than the wavelength of observation λ, and this regime is classified as large scale surface roughness. Most of the attention of this chapter will be devoted to this regime.

The second regime consists of roughness on the order of a wavelength λ in size, which shall be classified as intermediate scale surface roughness Under some circumstances it is quite possible that this regime may substantially affect the polarization of lunar thermal emission. There seems, however, to be no adequate way to account analytically for roughness of the order of λ at the present time since the diffraction integrals are somewhat difficult to evaluate. The Fresnel equations presented in Chapter III are no longer valid since they assume no intermediate scale roughness. Empirical studies would perhaps be one way of approaching the problem.[15]

The third regime consists of roughness much smaller than λ. Small scale surface roughness should affect the polarization of lunar thermal emission very little, since the apparent surface would appear as a smoothed version of the actual surface.

A rough model for large scale surface roughness may be derived directly from the smooth model in Chapter III by employing a statistical geometric optics approach. Consider a rough surface consisting of tilted facets uniformly distributed over the surface. The surface is a plane in the mean and the dimensions of the facets are much greater than λ. In Fig. 9 a typical facet is pictured. A set of orthogonal coordinates x, y, and z are fixed at point P on the lunar surface. Recall that point P is identical to point P in Figs. 6, 7, and 8.

The tilted facet has a surface normal $\vec{n}_o$ which makes an angle α with $\vec{n}$, the surface normal for the mean (flat) surface. The facet is positioned by p and q, the slopes of the facet measured in y and x, respectively. Note that

$$p = \tan \varphi; \tag{28}$$

$$q = \tan \psi, \tag{29}$$

and

$$\alpha = \cos^{-1}\left(\frac{1}{\sqrt{1 + p^2 + q^2}}\right). \tag{30}$$

Both p and q are modeled as random variables that are zero in the mean, and we will assume both have an equal standard deviation of σ. Also, p and q are assumed to be independent with a jointly normal probability density function

$$f(p\ q) = \frac{1}{2\pi\sigma^2} \exp\left[- \left(\frac{p^2 + q^2}{2\sigma^2}\right)\right]. \tag{31}$$

For surfaces that are the result of a large number of repeated events occurring randomly over the surface, the Central Limit Theorem applies

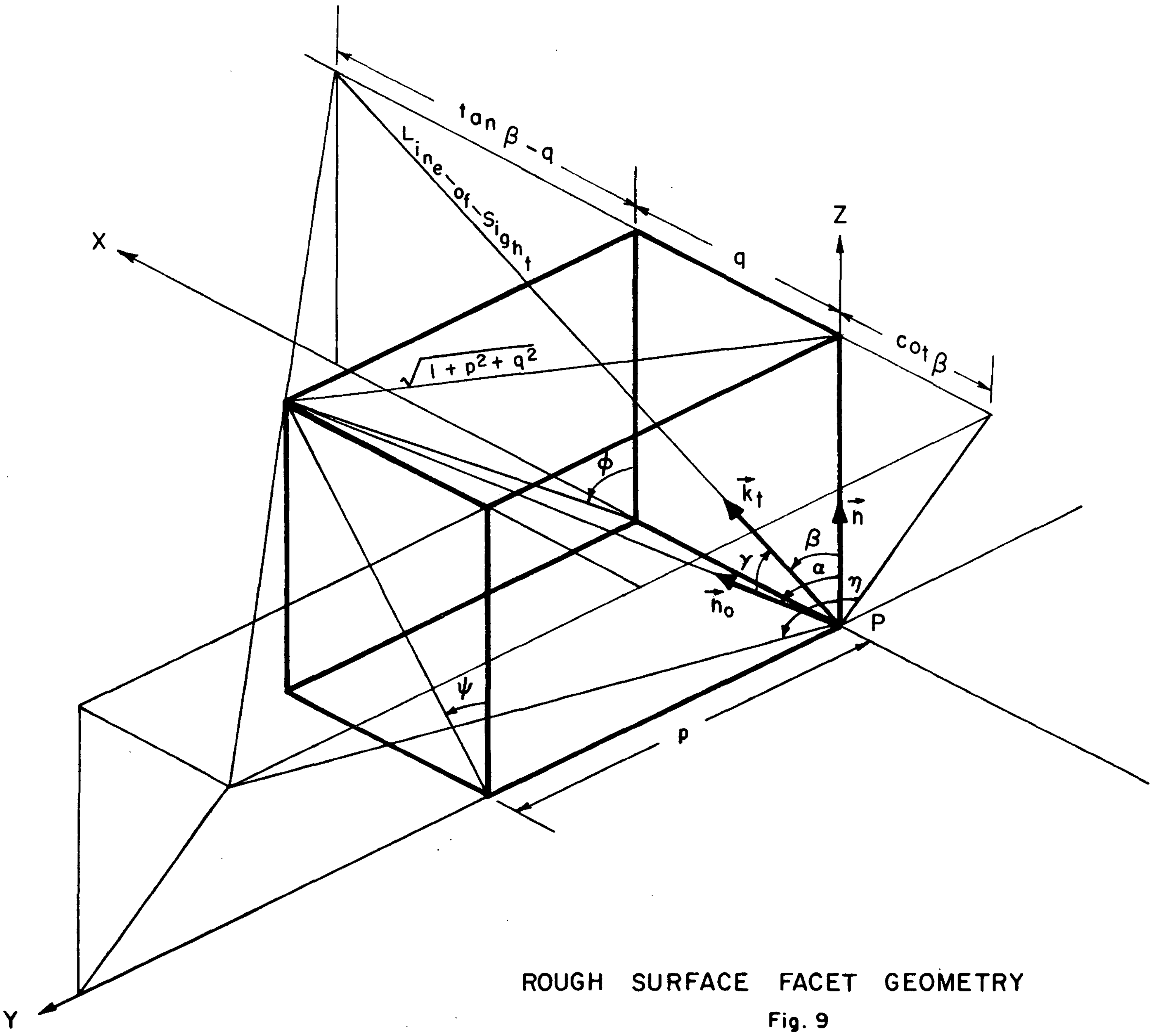

ROUGH SURFACE FACET GEOMETRY

Fig. 9

and insures a nearly normal probability density of surface heights.[16] Examples of some randomly repeated events that might occur on the lunar surface are meteorite impacts of various sizes and shapes and geological activity such as moonquakes and lava flows. If the effects of these randomly repeated events are distributed uniformly over the surface. the statistics will be homogeneous over the surface, and furthermore, if these events or processes operate without a preferred direction the statistics are isotropic over the surface.

Beckmann and Spizzichino[17] have shown that a surface which exhibits a normal probability density of surface heights also exhibits a normal probability density function of surface slopes. This tends to justify the use of Equation 31 here.

The angle γ is the true angle of transmission given by

$$\gamma = \cos^{-1}\left(\frac{\cos\beta + q\sin\beta}{\sqrt{1 + p^2 + q^2}}\right). \tag{32}$$

Here, β would be the angle of transmission if the facet was not tilted ($p = q = 0$). The plane of incidence for the tilted facet is the plane containing $\vec{n}_o$ and $\vec{k}_t$ while the plane of incidence for the smooth surface is the plane containing $\vec{n}$ and $\vec{k}_t$.

Recall that in Fig. 8, θ was the angle between the plane of incidence for the flat surface and the observer's plane of polarization. The rough surface, however, rotates the plane of incidence by an angle η as can readily be seen in Fig. 9, where

$$\eta = \cos^{-1}\left[\frac{1}{\sqrt{1 + \frac{p^2 (1 + \tan^2 \beta)}{(\tan \beta - q)^2}}}\right]. \tag{33}$$

Note that η is measured in a plane perpendicular to, and is the angle between, the plane of incidence for the smooth sphere (flat surface) and the plane of incidence for the rough sphere (tilted surface).

A surface exhibiting large scale roughness has two effects on the smooth model. The first effect is to change the angle of transmission for a flat surface to the corresponding angle for a tilted surface ($\beta \rightarrow \gamma$). The second effect is to rotate the plane of incidence by an additional angle η.

Substituting equations 32 and 33 into 18 and 19, one finds that

$$T_{P1}(\epsilon, \gamma, \theta, \eta) = T\left[\tau_{\parallel}(\epsilon, \gamma) \sin^2 (\theta + \eta) + \tau_{\perp}(\epsilon, \gamma) \cos^2 (\theta + \eta)\right], \tag{34}$$

and

$$T_{P2}(\epsilon, \gamma, \theta, \eta) = T\left[\tau_{\parallel}(\epsilon, \gamma) \cos^2 (\theta + \eta) + \tau_{\perp}(\epsilon, \gamma) \sin^2 (\theta + \eta)\right], \tag{35}$$

where $T_{P1}(\epsilon, \gamma, \theta, \eta)$ and $T_{P2}(\epsilon, \gamma, \theta, \eta)$ are now related to the random variables p and q.

A third effect of surface roughness is to create shadowing. Shadowing is a term used to describe the obscuring of the emission from a far facet by a closer facet.

For a statistically rough surface, a shadowing function $S(\sigma, \beta, q)$ is defined as the probability that the emission from a point on the rough surface characterized by σ, the standard deviation of surface slopes, and with a local slope of q, will not be shadowed at an angle of transmission β. A statistical model for $S(\sigma, \beta, q)$ developed by Smith[18] will be used in this study, but the details of the derivation of $S(\sigma, \beta, q)$ will not be given here. The function is

$$S(\sigma, \beta, q) = \frac{u(q + \cot \beta)}{1 + \Lambda}, \tag{36}$$

where $u(q + \cot \beta)$ is the unit step function given by

$$u(x) \triangleq \begin{cases} 0 & \text{for } x \leq 0 \\ 1 & \text{for } x > 0 \end{cases}, \tag{37}$$

and

$$\Lambda = \frac{\sqrt{2}\, \sigma \tan \beta}{2\sqrt{\pi}} \exp\left[-\left(\frac{1}{\sqrt{2}\, \sigma \tan \beta}\right)^2\right] - \frac{1}{2}\left[1 - \operatorname{erf}\left(\frac{1}{\sqrt{2}\, \sigma \tan \beta}\right)\right]. \tag{38}$$

Also,

$$\operatorname{erf}(x) \triangleq \frac{2}{\sqrt{\pi}} \int_0^x e^{-t^2}\, dt. \tag{39}$$

The shadowing function appears to satisfy one's intuition about rough surfaces since $S(\sigma, 0°, q) = 1$ (no shadowing is observed for a rough surface viewed normally), and $S(\sigma, 90°, q) = 0$ (total shadowing is observed for a rough surface viewed at grazing incidence).

The unit step function takes into account the fact that only a point on the rough surface with a local slope q less than the slope of the line-of-sight (cot β) can be observed from above. Also, the shadowing function is independent of the other local slope p, since the line-of-sight is measured in the same plane as q is measured.

Also, the derived shadowing function is in good agreement with the computer simulation of shadowing from a random rough surface by Brockelman and Hagfors[19]. This fact tends to justify the assumptions that Smith has made in his derivation. Fig. 10 shows

$$\overline{S(\sigma, \beta)} = \int_{-\infty}^{\infty} S(\sigma, \beta, q) \exp\left(\frac{-q^2}{2\sigma^2}\right) dq, \tag{40}$$

or

$$\overline{S(\sigma, \beta)} = \frac{\frac{1}{2}\left[1 + \mathrm{erf}\left(\frac{1}{\sqrt{2}\,\sigma \tan \beta}\right)\right]}{1 + \Lambda}, \tag{41}$$

where the bar superscript implies an expectation and $\overline{S(\sigma, \beta)}$ is the expected probability that point P on the rough surface characterized by σ, will not be shadowed at an angle of transmission of β, independent of surface height and local slopes p and q.

Taking into account shadowing, the expected value of Equations 34 and 35 are

$$\overline{T}_{P1}(\epsilon, \sigma, \beta, \theta) = \int_{-\infty}^{\infty} \int_{-\infty}^{\infty} S(\sigma, \beta, q)\, T_{P1}(\epsilon, \gamma, \theta, \eta)\, f(p, q)\, dp dq, \tag{42}$$

and

$$\overline{T}_{P2}(\epsilon, \sigma, \beta, \theta) = \int_{-\infty}^{\infty} \int_{-\infty}^{\infty} S(\sigma, \beta, q)\, T_{P2}(\epsilon, \gamma, \theta, \eta)\, f(p, q)\, dp dq, \tag{43}$$

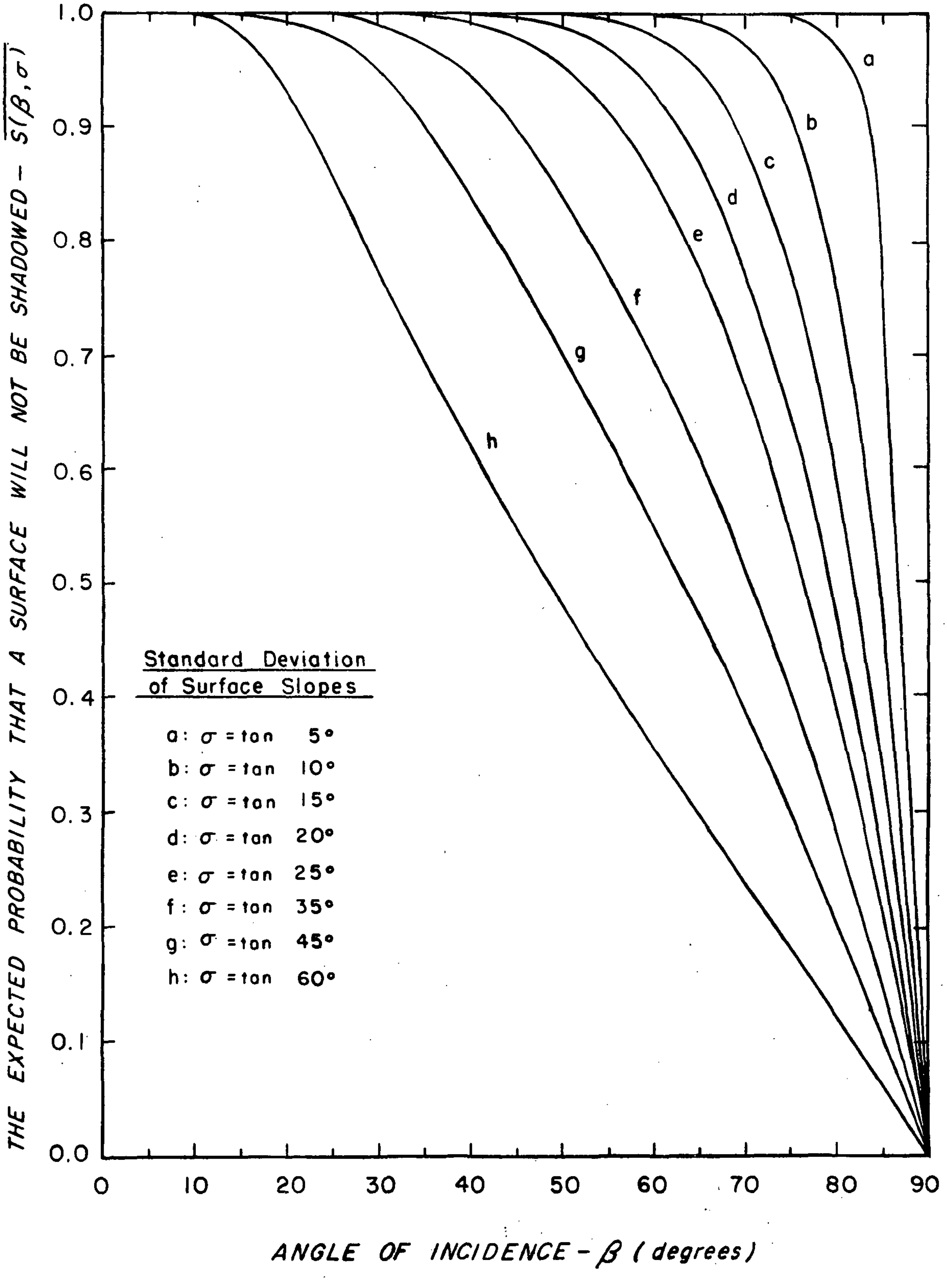

SHADOWING FUNCTION

Fig. 10

Taking full advantage of the symmetry of the integrand with respect to the random variable p and the unit step function, we have

$$\overline{T}_{P1}(\epsilon, \sigma, \beta, \theta) = \frac{2}{1+\Lambda} \int_{-\cot\beta}^{\infty} \int_{0}^{\infty} T_{P1}(\epsilon, \gamma, \theta, \eta)\, f(p, q)\, dp dq, \qquad (44)$$

and

$$\overline{T}_{P2}(\epsilon, \sigma, \beta, \theta) = \frac{2}{1+\Lambda} \int_{-\cot\beta}^{\infty} \int_{0}^{\infty} T_{P2}(\epsilon, \gamma, \theta, \eta)\, f(p, q)\, dp dq. \qquad (45)$$

Converting from angles β and θ to the distances r and d is accomplished by substituting Equations 17, 22, and 23 into Equations 44 and 45 so that functionally speaking

$$\overline{T}_{P1}(\epsilon, \sigma, r, d) = \overline{T}_{P1}(\epsilon, \sigma, \beta, \theta), \qquad (46)$$

and

$$\overline{T}_{P2}(\epsilon, \sigma, r, d) = \overline{T}_{P2}(\epsilon, \sigma, \beta, \theta). \qquad (47)$$

Equations 46 and 47 predict the noise-free linear polarization for a homogeneous, rough Moon (first regime) for an infinitely narrow beamwidth antenna that is linearly polarized in P1 and P2.

A possible source of error in the model arises if the Moon is not a good dielectric. This situation could be easily treated by introducing a complex dielectric constant given by

$$\epsilon = \epsilon' - j\frac{\sigma_2}{\omega} = \epsilon' - j\epsilon'', \qquad (48)$$

where ϵ' is now the real part of the dielectric constant; σ_2 is the nonzero conductivity of medium 2, and the radian frequency of observation is denoted by ω. For most substances that approximate the lunar soil, however, $\epsilon' \gg \frac{\sigma_2}{\omega}$ and the dielectric constant is very nearly a real quantity anyway. Basaltic powders, for example, have ϵ' at least 500 times greater than $\frac{\sigma_2}{\omega}$ at a wavelength of 1.2 cm.[20]

Also, if the relative permeability μ of the lunar soil is greater than unity, and there is no reason to believe that it is, then the relative refractive index between medium 2 and medium 1 can be defined as

$$n_{21} \triangleq \frac{1}{\sqrt{\mu\epsilon}} , \tag{49}$$

and n_{21} would simply replace ϵ in Equations 13 and 14.

There are two more important sources of error in the model, namely, the nonuniform heating of the lunar surface (phase effects denoted by $T(\beta, \theta)$) due to the Sun, and the existence of an inhomogeneous lunar surface (variations in the actual dielectric constant and/or changes in porosity). These errors are affected by antenna beam smoothing and will be discussed in more detail in Chapter V where beam smoothing is treated more extensively.

V. BEAM SMOOTHING

This chapter contains the derivation of the antenna response to the rough model obtained in the previous chapter using a Gaussian approximation for the measured antenna pattern. Equation 3 in Chapter II gave the response of the observer's antenna to the Moon's signal as the convolution of the lunar brightness temperature distribution with the normalized antenna power radiation pattern. Since the Moon is small in angular extent (approximately 0.5°), and the half power beamwidth of the antenna is smaller still (0.045°), then the spherical coordinate system may be replaced by a more convenient rectangular (x-y) coordinate system. Equation 3 now becomes

$$T_a(x',y') = \frac{1}{\Omega_a} \underset{\text{source}}{\int\int} T_s(x,y)\, P_n(x-x',y-y')\, dxdy, \qquad (50)$$

where x and y now correspond to hour angle and declination, respectively.

The normalized power radiation pattern for the 4.88 meter parabolic reflector at 3.1 mm wavelength can be fairly well approximated by a two dimensional Gaussian function of the form

$$P_n(x-x',y-y') = \exp\left\{-\ln 2\left[\left(\frac{x-x'}{W_x}\right)+\left(\frac{y-y'}{W_y}\right)^2\right]\right\}, \qquad (51)$$

where $2W_x$ and $2W_y$ are the half power beamwidths in hour angle and declination, respectively. In the function $P_n(x-x',y-y')$, the peak occurs at $x = x'$ and $y = y'$ and the half power curve is the ellipse described by the curve

$$\left(\frac{x-x'}{W_x}\right)^2 + \left(\frac{y-y'}{W_y}\right)^2 = 1. \tag{52}$$

Note also that Equation 51 assumes that the semi-minor and semi-major axes of the half power ellipse are oriented along the hour angle and declination axes.

One advantage of this Gaussian approximation is that the values for $P_n(x-x', y-y')$ off the x or y axis are simply the product of the pattern in x times the pattern in y or

$$P_n(x-x', y-y') = P_{nx}(x-x')\, P_{ny}(y-y'), \tag{53}$$

where

$$P_{nx}(x-x') = \exp\left[-\ell n\, 2 \left(\frac{x-x'}{W_x}\right)^2\right], \tag{54}$$

and

$$P_{ny}(y-y') = \exp\left[-\ell n\, 2 \left(\frac{y-y'}{W_y}\right)^2\right]. \tag{55}$$

The antenna solid angle, Ω_a now becomes

$$\Omega_a = \Omega x \Omega y, \tag{56}$$

where

$$\Omega_x = \int_{-\infty}^{\infty} P_{nx}(x)\, dx = W_x \sqrt{\pi/\ell n\, 2}, \tag{57}$$

and

$$\Omega_y = \int_{-\infty}^{\infty} P_{ny}(y)\, dy = W_y \sqrt{\pi/\ln 2} \; . \tag{58}$$

Suppose scans in hour angle are taken through the apparent center of the Moon (along a lunar diameter). Because of the circular symstry of the model the brightness temperature is symmetrical in y about the lunar diameter. In practive W_x and W_y are very small compared to the brightness temperature distribution in y and therefore the antenna measures an approximately constant temperature in y and

$$T_s(x, y) \approx T_s(x). \tag{59}$$

Equation 50 now becomes

$$T_a(x') = \frac{1}{\Omega_x} \int_{\text{source}} T_s(x)\, P_{nx}(x-x')\, dx \, . \tag{60}$$

Accordingly, Equations 48 and 49 can now be easily convolved using the above equation so that (letting r and r′ replace x and x′) we have

$$\overline{T}_{aP1}(\epsilon, \sigma, r', d) = \frac{1}{\Omega_1} \int_{\text{source}} T_{P1}(\epsilon, \sigma, r, d)\, P_{n1}(r-r')\, dr, \tag{61}$$

and

$$\overline{T}_{aP2}(\epsilon, \sigma, r', d) = \frac{1}{\Omega_2} \int_{\text{source}} T_{P2}(\epsilon, \sigma, r, d)\, P_{n2}(r-r')\, dr, \tag{62}$$

where Ω_1 and Ω_2 are the antenna angles (no longer solid angles) measured in hour angle for polarization positions P1 and P2, respectively. Also, $P_{n1}(r-r')$ and $P_{n2}(r-r')$ are the normalized power radiation patterns measured in hour angle for P1 and P2, respectively, where

$$P_{n1}(r-r') = \exp\left[-\ln 2\left(\frac{r-r'}{W_1}\right)^2\right], \tag{63}$$

and

$$P_{n2}(r-r') = \exp\left[-\ln 2\left(\frac{r-r'}{W_2}\right)^2\right], \tag{64}$$

where $2W_1$ and $2W_2$ are the half power beamwidths measured in hour angle for polarization positions P1 and P2. The linear polarization positions are achieved by a simple rotation of the linearly polarized feed as shown in Fig. 2.

An experimental verification of beam ellipticity $(W_1 \neq W_2)$ is accomplished by taking drift scans across the center of the quiet Sun in polarization positions P1 and P2. Since radiation from the quiet Sun is thought to be unpolarized, the difference between the measured polarizations in P1 and P2 should be due to the unequal antenna patterns in P1 and P2. This false difference of polarizations will be called pseudo-polarization. Figs. 11 and 12 show the pseudo-polarization of the quiet Sun on two separate occasions. Polarization differences of 1 to 2 percent relative to the central disk temperature are observed for beamwidths $(2W_1$ and $2W_2)$ that are as close as .002°! Since the peak percent polarization for lunar thermal emission is only about 3 to 4 percent at the limbs at 3.1 mm, pseudo-polarization is an important effect to consider in analyzing the lunar data. Pseudo-polarization effects can be accounted for by assuming unequal half power beamwidths in the convolutions of the antenna beam with the rough lunar model.

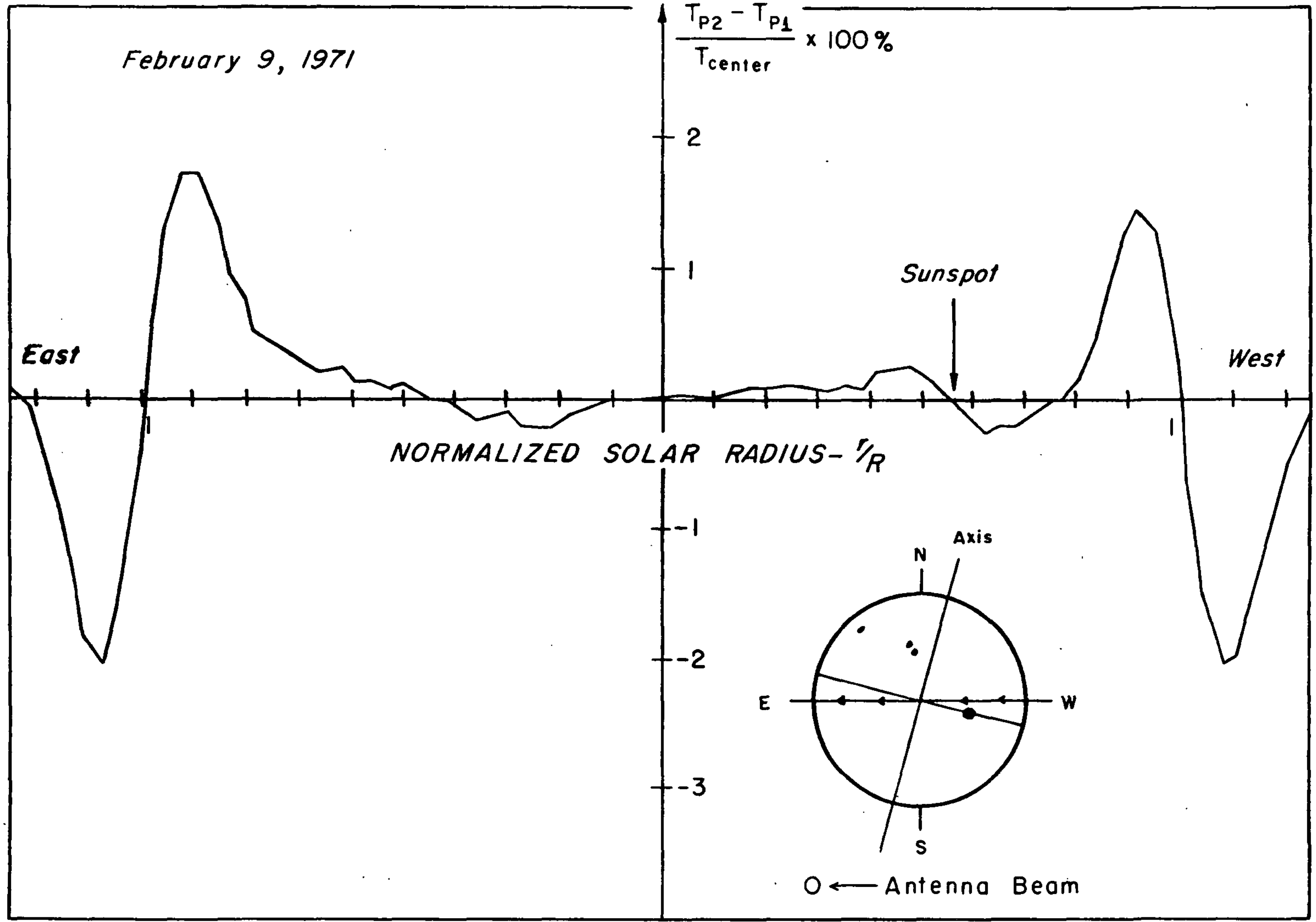

ANTENNA PSEUDO-POLARIZATION FOR THE QUIET SUN

Fig. 11

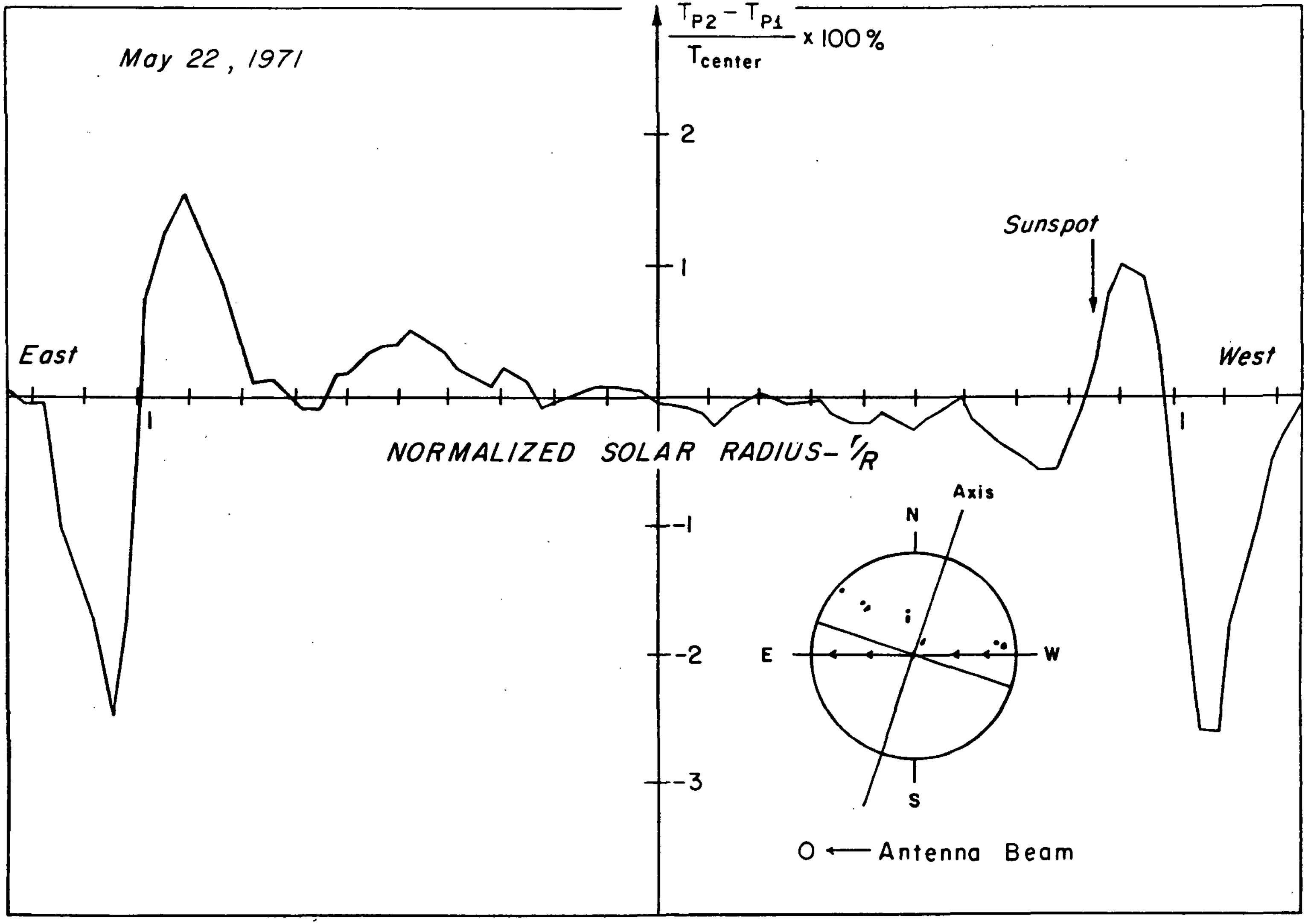

ANTENNA PSEUDO-POLARIZATION FOR THE QUIET SUN

Fig. 12

The percent lunar polarization for the rough model is defined for the disk of the Moon as

$$\%\mathrm{Pol}(\epsilon, \sigma, r', d) \triangleq \frac{\overline{T}_{aP2}(\epsilon, \sigma, r', d) - \overline{T}_{aP1}(\epsilon, \sigma, r', d)}{\overline{T}_{aP2}(\epsilon, \sigma, r', d) + \overline{T}_{aP1}(\epsilon, \sigma, r', d)} . \qquad (65)$$

In Fig. 13 a three dimensional plot of the linear percent polarization is shown with variations in the effective dielectric constant, the standard deviation of the surface slopes, and the normalized apparent lunar radius. A mean lunar radius of 1738 km and a mean Earth-Moon separation of 384,400 km were used to calculate a mean lunar parallax ρ (see Chapter III Equation 15). Values for $2W_1$ and $2W_2$ are .045° and .0435°, respectively.

If the antenna beam misses the apparent center of the Moon by a small distance d (normalized to an apparent lunar radius), as pointed out in Chapter III, then the variation of the %Pol with d must be investigated as shown in Fig. 14. Notice that the %Pol is a negative quantity near the center of the disk for a non zero value of d. This implies that the excess linear polarization is normal to the path of the scan. Normally, the %Pol is a positive quantity implying that the excess linear polarization is parallel to the path of the scan.

The distance d must be kept small or the symmetry properties of the polarization about the path of the scan will not hold true. The symmetry condition was necessary, recall, for the approximation of the two-dimensional convolution (Equation 52) as a one-dimensional convolution (Equation 62).

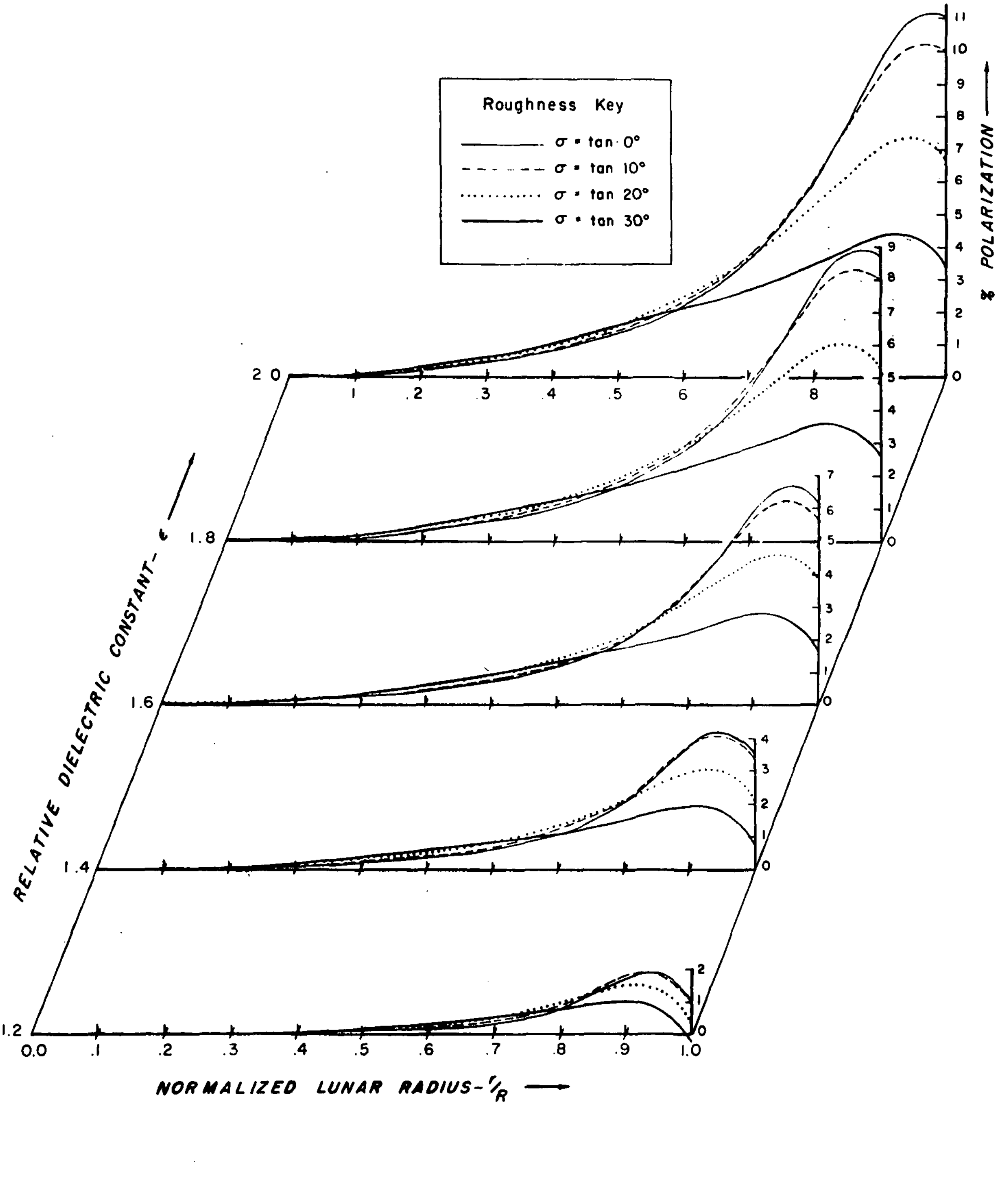

LINEAR PERCENT POLARIZATION FOR A ROUGH MOON

Fig. 13

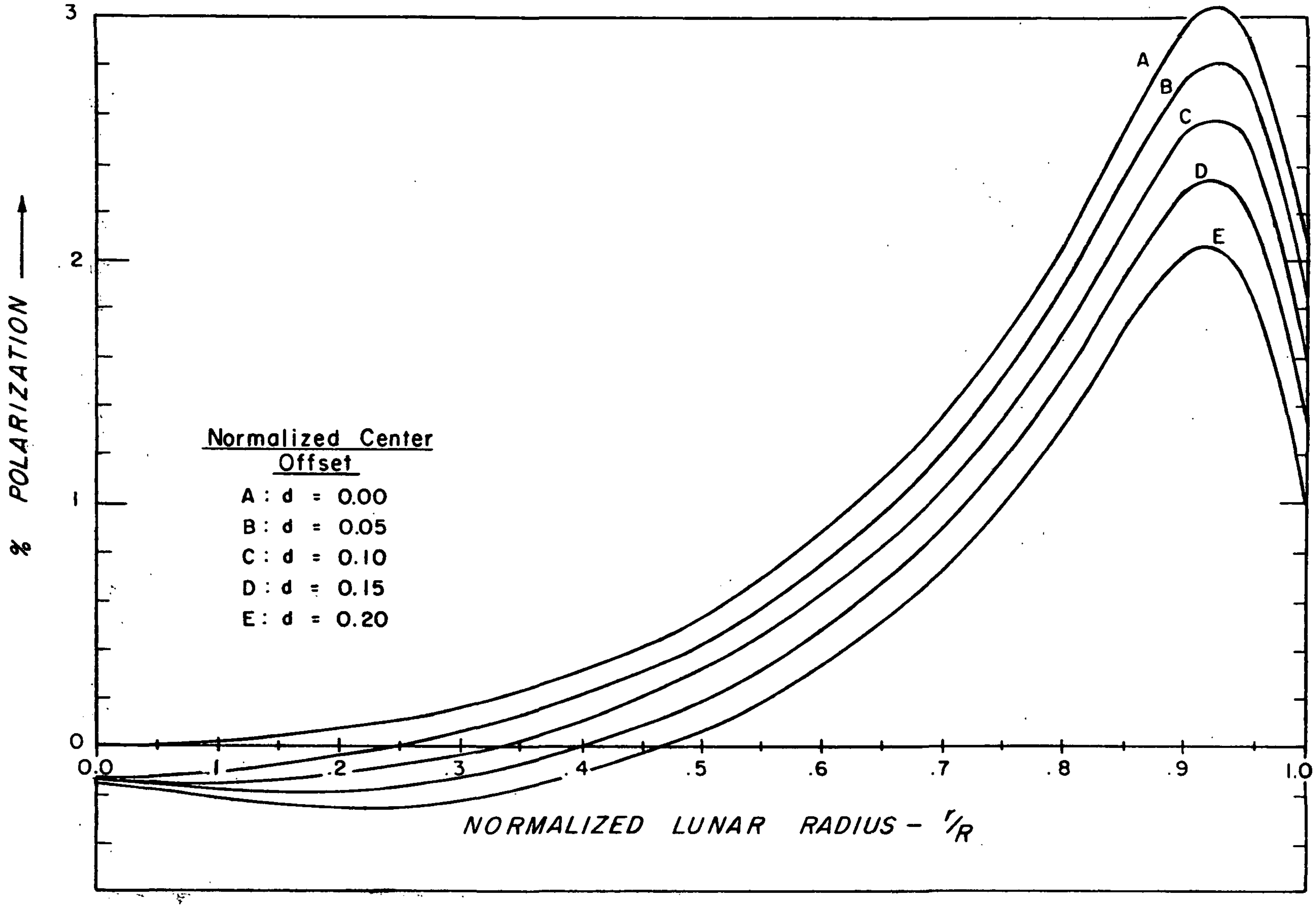

LINEAR PERCENT POLARIZATION VERSUS CENTER OFFSET FOR $\epsilon = 1.4$ AND $\sigma = \tan 20°$

Fig. 14

Fortunately, the percent polarization is a quantity that is relatively insensitive to temperature variations across the lunar disk. This is due to the fact that the numerator and denominator of Equation 65 are both proportional to the surface temperature by approximately the same factor and their ratio, therefore, tends to be very weakly dependent upon temperature. To verify this fact, the percent polarization for a linearly varying temperature distribution was compared to the percent polarization for a constant surface temperature. Since the maximum relative error between the two models is less than one percent, the effect of surface temperature variations on the percent polarization can be regarded as negligible compared to the noise in the data.

Another possible source of error may arise from the fact that the lunar surface may not be entirely homogeneous. Variations in ϵ over the surface could be due to actual variations in the type of material observed (highland regions may have a higher ϵ than maria regions for example).

The average half power beam area projected on the Moon is roughly 70,000 km^2, the effective area over which the main beam weights and averages the surface inhomogeneities. Surface irregularities much less than 70,000 km^2 in extent would be averaged over to some mean value and their effect on the data would not be appreciable.

VI. EQUIPMENT AND EXPERIMENTAL PROCEDURE

This chapter contains a brief description of the equipment and the data taking procedure used in this study.

The University of Texas Millimeter Wave Observatory is located on Mt. Locke near Fort Davis, Texas. The location is ideal since the atmospheric attenuation due to water vapor is low owing to the dry climate and high altitude (2070 meters).

The prime instrument of the Observatory is a 4.88 meter diameter parabolic reflector. At 3.1 mm the 3 dB beamwidths are .045° in hour angle and .0435° in declination. The principle sidelobes in the hour angle and declination planes are at least 20 dB down and the cross polarization sidelobes are at least 25 dB down. The procedure for measuring the antenna pattern is to point the antenna at a transmitter site located approximately 13 km away. The "pattern range" was particularly good in that the reflections from the surrounding terrain were minimal due to the particular properties of the range, which have been reported by Cogdell.[21]

The antenna is supported by an equatorial mount as shown in Fig. 1. The entire structure is enclosed in a steel astrodome to protect the antenna and equipment from the weather.

The antenna is positioned by servo systems with digital readouts to .001°. Sag, axis tilts, and atmospheric refraction have been corrected for in an ephemeris used for locating radio sources. The peak pointing errors of the antenna are less than .006°. A more detailed description of the antenna system is given by Tolbert, Straiton, and Krause[22]. A thorough evaluation of the antenna's performance by Davis and Cogdell[23], and Davis[24] has been made, and the results indicate that the antenna ranks with the best in its peer group.[25]

The receiver used in this study is a 3.1 mm (97.1 GHz) superheterodyne radiometer schematically shown in Fig. 15. The receiver consists of an RF mixer and IF amplifier located at the prime focus of the dish followed by a lock-in amplifier located in an observation room in the dome. The $\Delta T_{rms}|_{\tau=1\ \mathrm{sec}}$ of the receiver was approximately 5.0°K for the lunar data.

Six sets of lunar polarization data were taken from February to March 1971. Table 1 shows the relevant lunar physical observations for each of the six data sets. Values for the apparent lunar semidiameter (radius) and the velocity of the Moon with respect to the Earth were obtained from an ephemeris already in existence. Values for the phase and tilt for 0 hrs. Universal Time (U.T.) were obtained with the American Ephemeris and Nautical Almanac.[26]

The data was taken under conditions of optical visibility with little or no surface winds present to introduce pointing errors. Drift scans of the Moon were favored because of the constant tracking rate produced. This eliminated any variation in tracking that would produce rapid changes in antenna temperature at the limbs of the Moon.

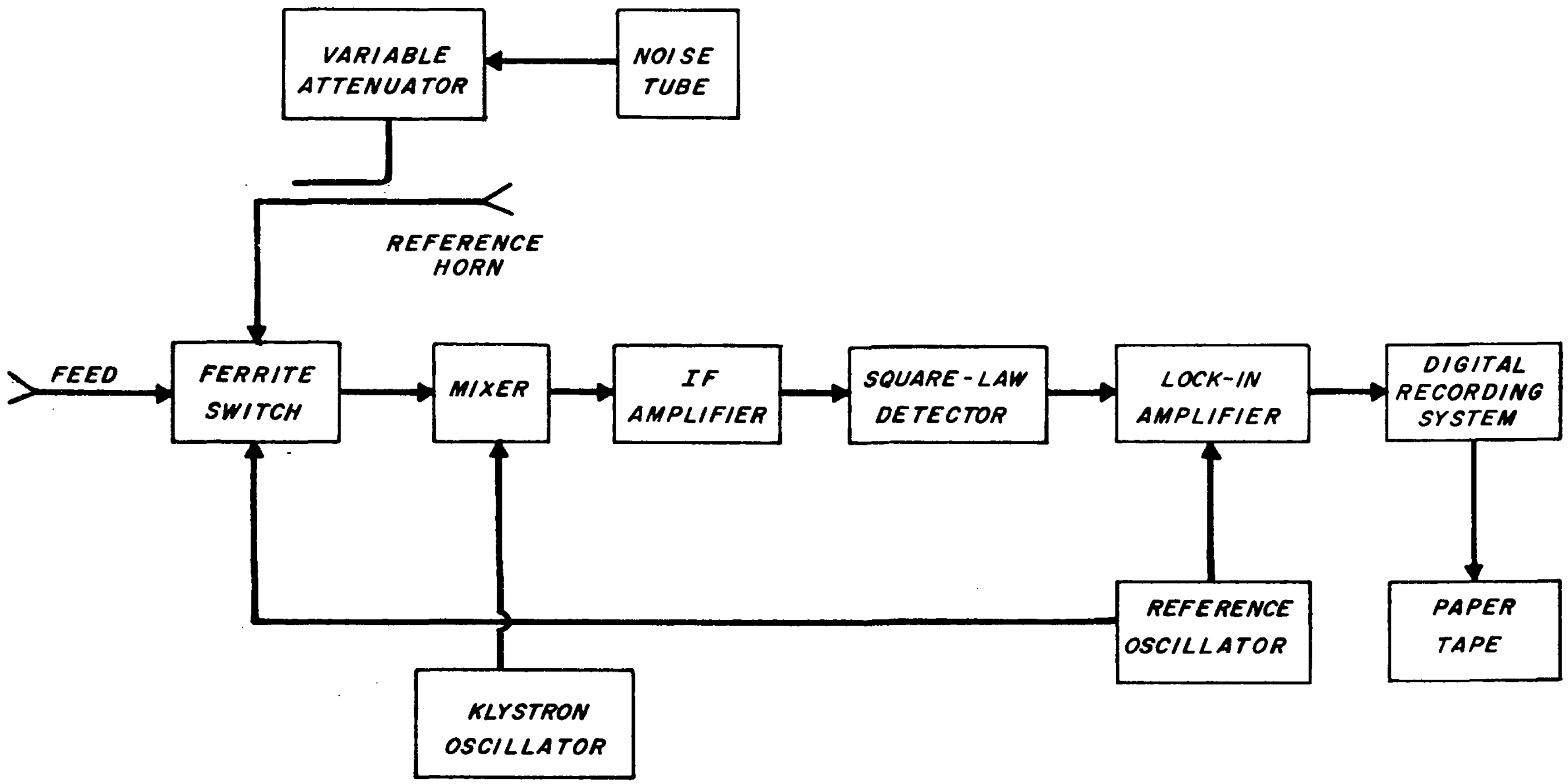

RECEIVER CIRCUIT

Fig. 15

LUNAR OBSERVATIONS

Data Set No.	Date Mo/Day/Yr	Start Time[u]	Stop Time[u]	Total No. of Scans	Relevant Physical Observations for the Moon				
					Age[o] since new Moon (days)	Axis Tilt[o] (°)	Apparent Semi-diameter x(.001°)	Center Offset[n] +north -south	Velocity (.001°-sec^{-1})
1	2/9/71	03:17	06:19	48	13.0	12.65	248.2±.1	+0.02±.01	4.09±.01
2	2/20/71	12:07	16:40	64	24.0	5.79	262.7±.1	-0.09±.01	4.06±.01
3	2/25/71	16:20	21:07	64	29.0	340.97	278.7±.1	+0.00±.01	4.08±.01
4	3/4/71	23:24	02:44	48	6.6	351.42	256.3±.1	+0.14±.01	4.07±.01
5	3/20/71	09:16	12:16	48	22.6	2.02	260.9±.1	-0.10±.01	4.05±.01
6	3/26/71	15:19	20:12	64	28.6	338.02	278.6±.1	+0.06±.01	4.07±.01

All confidence limits are approximately two standard deviations

[u] Measured in Universal Time

[o] For 0 hours Universal Time

[n] Normalized to an apparent lunar semidiameter

Table 1

The antenna feed was set up in the P1 polarization position (see Fig. 2), and the antenna was pointed at a location 0.75° west of the apparent center of the Moon. With the antenna fixed, the data scan was initiated and the Moon was allowed to drift through the antenna beam till the Moon was 0.75° east of the beam and then the data scan was terminated. This process was repeated three more times in P1, then the polarization was changed to P2 and four more drift scans were obtained. In this way equal numbers of drift scans in P1 and P2 were acquired till either a sufficient amount of data had been obtained or bad weather forced termination of the data taking.

An integration time of 4 seconds was used, giving a spacing between data points of roughly .016° or 1/3 beamwidth. A longer integration time of 10 seconds was available and would have increased the receiver sensitivity, but sampling would have smoothed the data undesirably.

The digitized data was punched out on coded paper tape for later conversion to punched computer cards. The data was analyzed on the CDC 6600 high speed digital computer in operation at The University of Texas at Austin.

VII. DATA ANALYSIS

This chapter describes the data analysis scheme and briefly discusses some of the numerical techniques employed. The main goals in analyzing the data are to minimize the receiver noise present, and to display the final results in such a way as to lend insight into the behavior of the linear polarization of lunar thermal emission at 3.1 mm wavelength. The raw data, in the form of punched computer cards, is analyzed by a computer program that outputs the linear percent polarization data versus a normalized lunar radius. Another program least squares fits the final rough model (Equation 65) to the linear percent polarization data. The outputs from this program are values for ϵ, the effective dielectric constant, and σ, the standard deviation of surface slopes, along with confidence limits for both parameters.

To begin with, a straight line is least squares fitted to the two baselines on either side of the Moon's signal for each drift scan. The fitted line is then subtracted from the scan to remove any receiver drift and offset that may be present. A linear model is used here because the baseline drift of the 3.1 mm radiometer is small and nearly linear during one drift scan (approximately 6 minutes).

Many scans are averaged in both the P1 polarization position and the P2 polarization position so that the receiver noise can be reduced significantly. The averaging process requires that the apparent centers be known in order for the averaging to be done on ordinates with identical abscissas relative to the centers of the scans. In this connection a model that approximates a scan across a lunar diameter was developed to locate the centers of the scans. The center of each scan was obtained by least squares fitting the model to the scan.

First, a simplified model for $T_s(x)$, the lunar brightness temperature, is assumed to be of the form (see Fig. 16)

$$T_s(x) = (T_c + mx)\left[u(x + x_\ell) - u(x - x_\ell)\right], \tag{66}$$

where T_c is the average temperature of the lunar disk (also the central disk temperature); m is the slope of the brightness temperature distribution across the lunar disk; x is the abscissa coordinate (zero at the center); x_ℓ is the distance measured from the center to the limb and u is the unit step function.

A Gaussian approximation for $P_n(x)$, the normalized power radiation pattern of the antenna in one dimension, is

$$P_n(x) = \exp\left[-\ell n\, 2\left(\frac{x}{W}\right)^2\right], \tag{67}$$

where, as before, 2W is the half power beamwidth measured in x.

Using Equation 52 in Chapter V, T_a, the antenna response, is simply the convolution of Equation 66 with Equation 67 which is

$$T_a(x') = \frac{1}{2}\left[m\left(x'-x_c\right) + T_c\right]\left[\operatorname{erf}\left(\frac{x'-x_c+x_\ell}{W/\sqrt{\ell n\, 2}}\right) - \operatorname{erf}\left(\frac{x'-x_c-x_\ell}{W/\sqrt{\ell n\, 2}}\right)\right]$$

$$+ \frac{mW}{2\sqrt{\pi\, \ell n\, 2}}\left\{\exp\left[-\left(\frac{x'-x_c+x_\ell}{W/\sqrt{\ell n\, 2}}\right)^2\right] - \exp\left[-\left(\frac{x'-x_c-x_\ell}{W/\sqrt{\ell n\, 2}}\right)^2\right]\right\}, \tag{68}$$

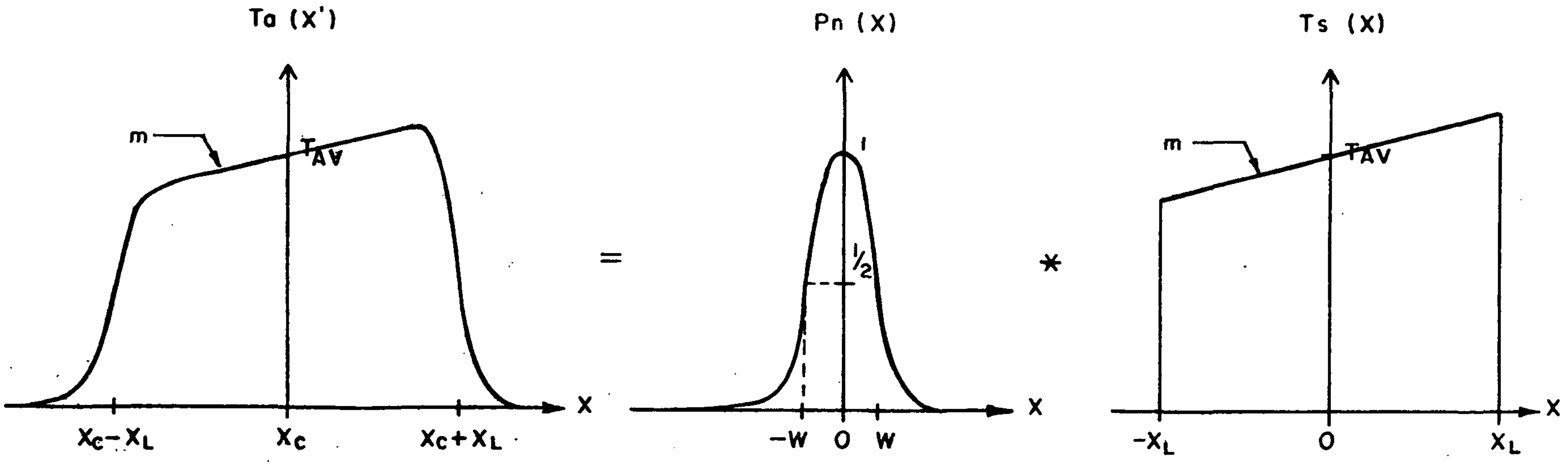

* — Convolution

$$Ta\,(X') = \frac{1}{\Omega x} \int_{-\infty}^{\infty} Ts\,(X)\; Pn\,(X - X')\; dX$$

ONE DIMENSIONAL CONVOLUTION OF A GAUSSIAN ANTENNA BEAM WITH AN APPROXIMATE LUNAR TEMPERATURE DISTRIBUTION

Fig. 16

where x_c is now defined as the location of the apparent center and x' represents the abscissa coordinate in the data plane. For clarity, the scan model represented by the above equation is shown along with $T_s(x)$ and $P_n(x)$ in Fig. 16. The scan model determines x_c to within an average maximum uncertainty of ±.003°. The other parameters determined by the model are m, T_c, x_ℓ, and W which are used to achieve a good least squares fit to the scan.

Once the centers of the scans are located, a new set of abscissas is defined for all scans with $x' = 0$ at the center. This is because, in general, the scan centers will not be in the same location for each scan. A new set of ordinates is obtained for the newly defined abscissas by linearly interpolating between successive pairs of the old ordinates. This allows the averaging to be done on the ordinates with common abscissas for all scans. The linear interpolation also reduces slightly the receiver noise present in the data.

After the scan center is determined and before the scan is averaged with others, the scan is normalized at its central ordinate by first averaging the central ordinate with a point on either side to reduce the uncertainty. This average is then divided into to the entire scan for the proper normalization. This process is done for both the P1 and P2 scans since the lunar thermal emission at the apparent center is approximately unpolarized due to spherical symmetry. The normalization procedure eliminates the need for an absolute temperature calibration for the scan since the data point numbers are now relative to the normalized central disk temperature.

Each data scan is analyzed in the above fashion and stored according to the polarization position (either P1 or P2) for averaging to reduce noise fluctuations. The data in P1 is then subtracted from the data in P2 and this difference is then divided by the sum of the P1 and P2 data, point by point, to simulate the final linear percent polarization model derived in Chapter V (see Equation 65).

The abscissas are normalized to an apparent lunar radius for easy comparison between data sets taken at times when the Moon was at different distances from Earth.

Chapter V showed that the linear percent polarization (sometimes referred to as the degree of linear polarization) was relatively insensitive to lunar phase effects. Another advantage of displaying data as a linear percent polarization is that this quantity is less sensitive to noise than a simple difference of polarizations ($T_{aP2} - T_{aP1}$) as shown in Appendix B.

Estimates of ϵ and σ are obtained by least squares fitting the nonlinear model in Equation 65 to each of the six data sets. Appendix B shows that the i^{th} residual of the model regression (assuming that the model is correct) has a value given by

$$S_{\%}(x_i) = \frac{\sqrt{\sigma_1^2 + \sigma_2^2}}{2\,T_{av}(x_i)}\,, \tag{69}$$

where σ_1^2 and σ_2^2 are the variances of the noise for the final averaged P1 and P2 polarization scans, respectively. Since $S_{\%}$ varies over the lunar disk as a function of x_i, weighted least squares are used to weight each data point of the percent polarization proportional to $T_{av}(x_i)$, the average polarization signal.

The model for the percent polarization in Equation 65 is said to be intrinsically nonlinear, that is, the form of the model is nonlinear in the model parameters ϵ and σ, regardless of any transformation attempt to achieve a linear model (linear in ϵ and σ). There are many techniques that are currently used to obtain parameter estimates for intrinsically nonlinear models but we shall only discuss three relevant methods here.

The linearization method uses a Taylor series expansion of the nonlinear model where the expansion is curtailed at the first partial derivatives of the model with respect to each model parameter. The expansion is now a linear model form to the order of the approximation and the parameter estimates can be obtained by standard linear least squares estimation theory. The linearization procedure has several possible drawbacks for some nonlinear models, namely, the sum of squares (defined as the sum of the squares of the differences between the observed data and model prediction) may converge very slowly, oscillate wildly, or diverge altogether.

The steepest descent method concentrates on minimizing the function representing the sum of squares for the nonlinear model. Starting with the sum of squares for a point in parameter space, several different sum of squares are calculated by selecting several different combinations of model parameters. The evaluated sum of squares are now treated as observations of a dependent variable and the combinations of model parameters are treated as observations of the corresponding independent variable. A plane is now fitted to the surface defined by the sum of squares using linear least squares techniques which gives an indication as to which direction to move in order to maximize the decrease in the sum of squares function. While, theoretically, the steepest descent method will converge the sum of squares, it may do so in practice with agonizing slowness after some rapid initial progress.

The method used to obtain estimates of ϵ and σ in this study is known as Marquardt's compromise.[27] This method appears to enlarge on the number of nonlinear models that can be handled by nonlinear estimation and represents a compromise between the linearization method and the steepest descent method, combining the best features of both while avoiding their most serious limitations. Suppose from an initial point in parameter space the steepest descent technique gives a vector in that space which represents the best local direction for movement to obtain smaller values for the sum of squares. This local direction, however, may not be the best overall direction because of the inherent nonlinear properties of the model. The application of the linearization method leads to another vector in parameter space that is less than 90° from the first vector. The Marquardt algorithm provides a method for interpolating between the two vectors to achieve an optimum reduction in the sum of squares. The details of his method will not be given here; however, a discussion of Marquardt's compromise can be found in the previously quoted reference and a more complete introduction to nonlinear estimation theory is given by Draper and Smith[28].

Two versions of a basic library program by Marquardt and Stanley[29] employing Marquardt's compromise are used in this study. The first version was used to fit the scan model in Equation 68 to the data in order to locate the scan centers.

The second version employs weighted nonlinear least squares and is used to obtain values for ϵ and σ from the percent polarization data.

The numerical integrations of the rough model in Equations 44 and 45 were done with a subroutine that employs a modified Simpson's rule to evaluate the integrals between the appropraite limits. The interval is divided successively into thirds until a set convergence criterion is met. Since the subroutine operates on only 1/3 of the interval on any given level, it has the ability to concentrate points only in those portions of the interval where the slope of the integrand is varying rapidly. For a given accuracy, this method uses only about 1/5 the number of points used in an equal-interval type of Simpson's rule. The fewer the number of points used, the less time will be required for the integrations.

A description of the confidence limits on ϵ and σ together with a discussion of the experimental errors and results is given in the next chapter.

VIII. RESULTS AND CONCLUSIONS

This chapter summarizes the various sources of experimental error along with the results of the data analysis scheme. The experimental results are compared to those of previous workers in this field.

Receiver noise was the main source of experimental error encountered in this study. This necessitated the averaging of anywhere from 24 to 48 drift scans in each of the two polarization positions to reduce the noise to acceptable levels. The final receiver noise present in the linear percent polarization data for each data set is expressed in the same units as the linear percent polarization and is listed in Table 2. Also, the greatest amount of noise reduction is achieved when the linear percent polarization of lunar thermal emission is expressed as a ratio of the difference over the sum of the two orthogonal polarizations (see Appendix B).

The absolute pointing errors of the antenna are very small at .006° peak. There was a systematic offset from the apparent center of the Moon for some of the data sets. This offset was not due to systematic antenna pointing errors but was caused by an error in the ephemeris. Initially, all data was obtained by making drift scans through the sub Earth point on the Moon. Later, however, it was realized that the correct point for the drift scan to intersect was the apparent center. It should be pointed out that the mean center is simply the average position of the sub Earth point over a lunation, and the two points do

EXPERIMENTAL RESULTS

Data Set Number	Relevant Physical Observation for the Moon			Estimated Receiver Noise[p] (%)	First Iteration		Second Iteration
	Center Offset[n] (+north / -south)	Age[o] since new Moon (days)	Fraction of Disk Illuminated		Effective Dielectric Constant[c] $\epsilon_{av}=1.37\pm.08$	Standard Deviation of Surface Slopes[c] (°) $\sigma_{av}=18°\pm2°$	Effective Dielectric Constant[c] $\epsilon_{av}=1.34\pm.08$ with $\sigma=\sigma_{av}$
1	+0.02±.01	13.0	0.98±.01	0.35	1.28±.04	16 ± 4	1.27±.03
2	-0.09±.01	24.0	0.29±.01	0.46	1.45±.05	19 ± 3	1.39±.02
3	+0.00±.01	29.0	0.01±.01	0.56	1.45±.09	25 ± 4	1.39±.04
4	+0.14±.01	6.6	0.60±.01	0.46	1.3±.2	24 ± 11	1.32±.04
5	-0.01±.01	22.6	0.46±.01	0.54	1.40±.03	10 ± 2	1.32±.03
6	+0.06±.01	28.6	0.00±.01	0.55	1.34±.04	14 ± 3	1.34±.03

[c] Confidence limits are approximately 95% confidence limits based on Snedecor's F-distribution (approximately two standard deviations)

[n] Normalized to an apparent lunar semidiameter

[o] For 0 hours universal time

[p] Expressed in units of the linear percent polarization (%Pol)

Table 2

not necessarily coincide at a given instant. The ephemeris was corrected to compute where in declination the antenna should have been pointed in order for the antenna beam to drift through the apparent center. From the old ephemeris coordinates the offsets were computed and the parameter d was created to take this systematic offset into account in the model (see Equation 65 and Fig. 14). For small d this source of error can be eliminated.

Another possible source of experimental error can arise if the antenna patterns in the P1 and P2 polarization positions are different (sometimes called beam ellipticity). Chapter V uses a specialized Gaussian approxmation of the antenna patterns to account for the pseudo-polarization effects due to beam ellipticity. The approximations should be sufficiently valid to eliminate beam ellipticity as a possible source of error.

Another general class of errors are due to the data analysis scheme. The maximum uncertainty in finding the centers of the lunar drift scans was about ±.003°. In practice, this source of error is negligible compared to the receiver noise.

The numerical approximations of the integrals in Equations 48 and 49 were done with sufficient accuracy (three significant digits for the linear percent polarization) to also make this possible source of error negligible compared to the receiver noise.

A typical drift scan profile along with the reduced percent polarization is shown in Figs. 17 to 28 for each of the six data sets. The

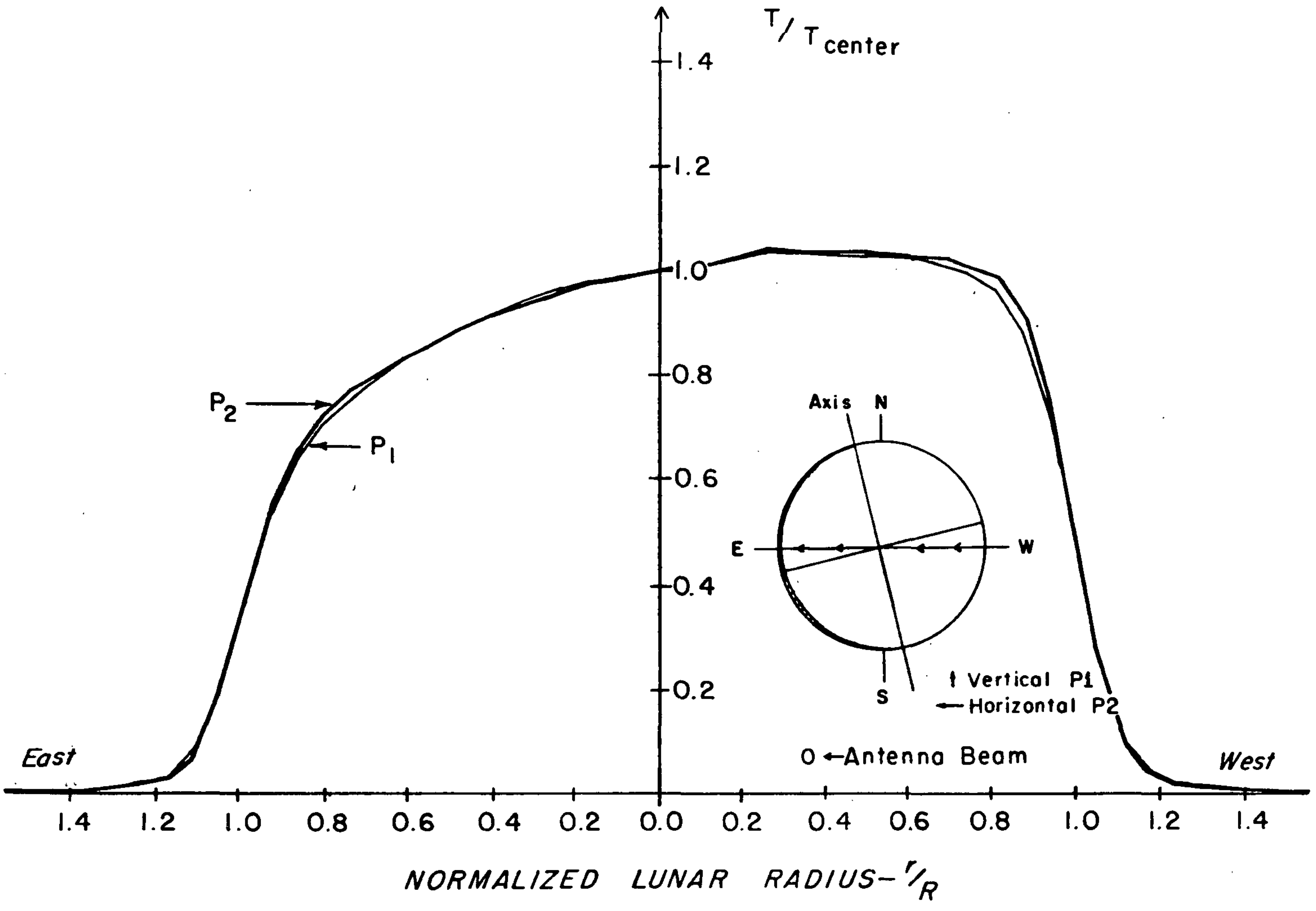

P1 AND P2 POLARIZATIONS FOR DATA SET NUMBER 1

Fig. 17

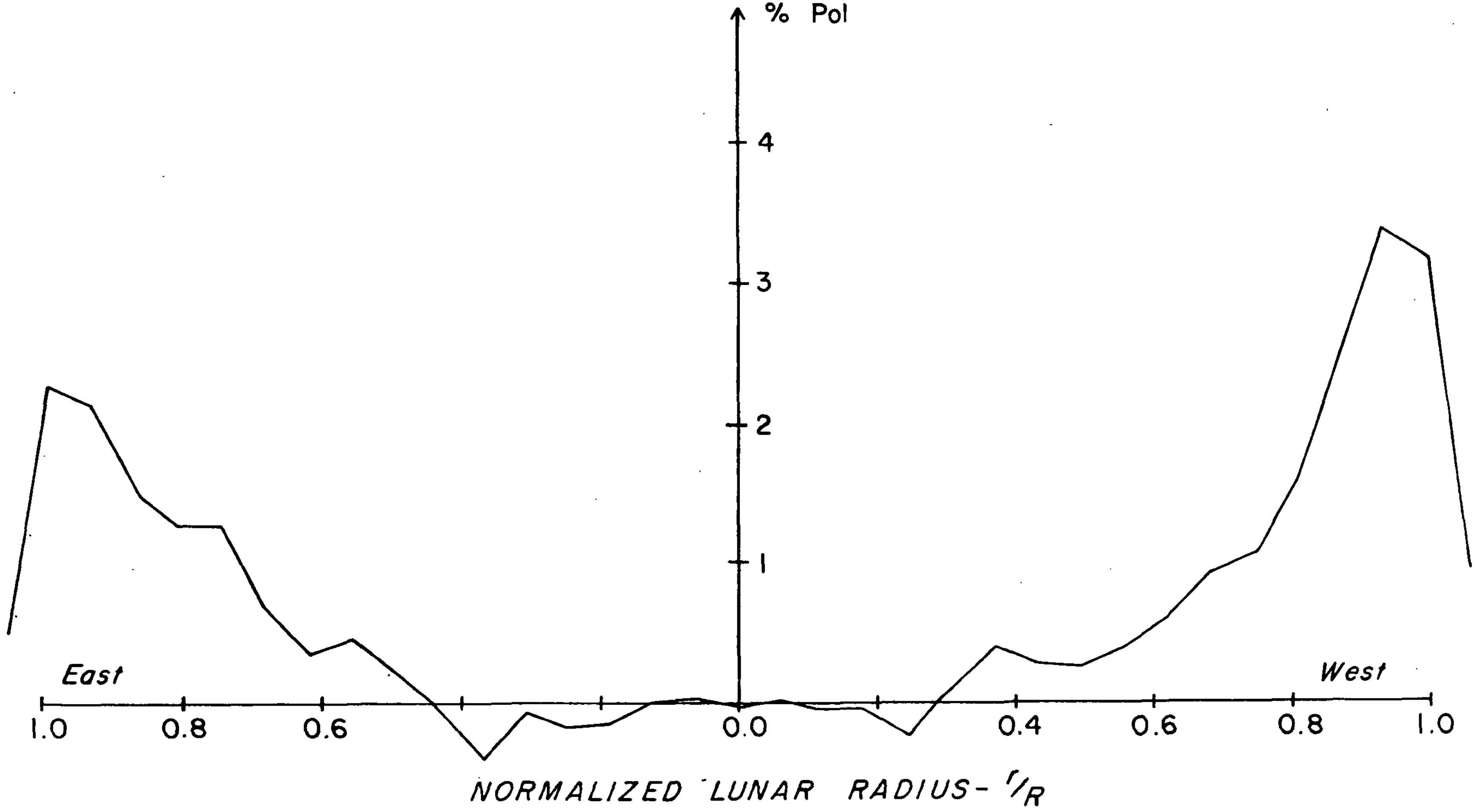

LINEAR PERCENT POLARIZATION FOR DATA SET NUMBER 1

Fig. 18

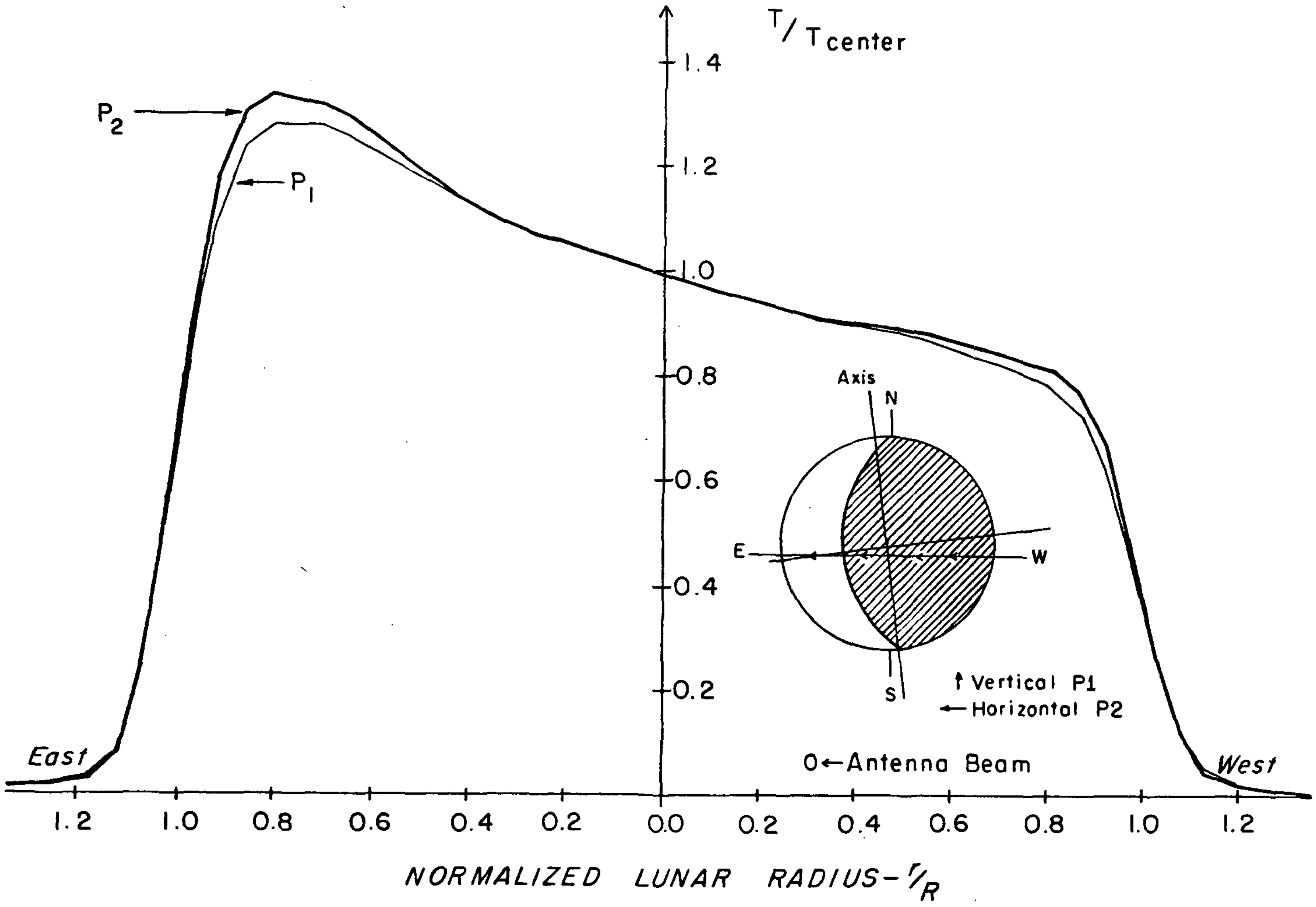

P1 AND P2 POLARIZATIONS FOR DATA SET NUMBER 2

Fig. 19

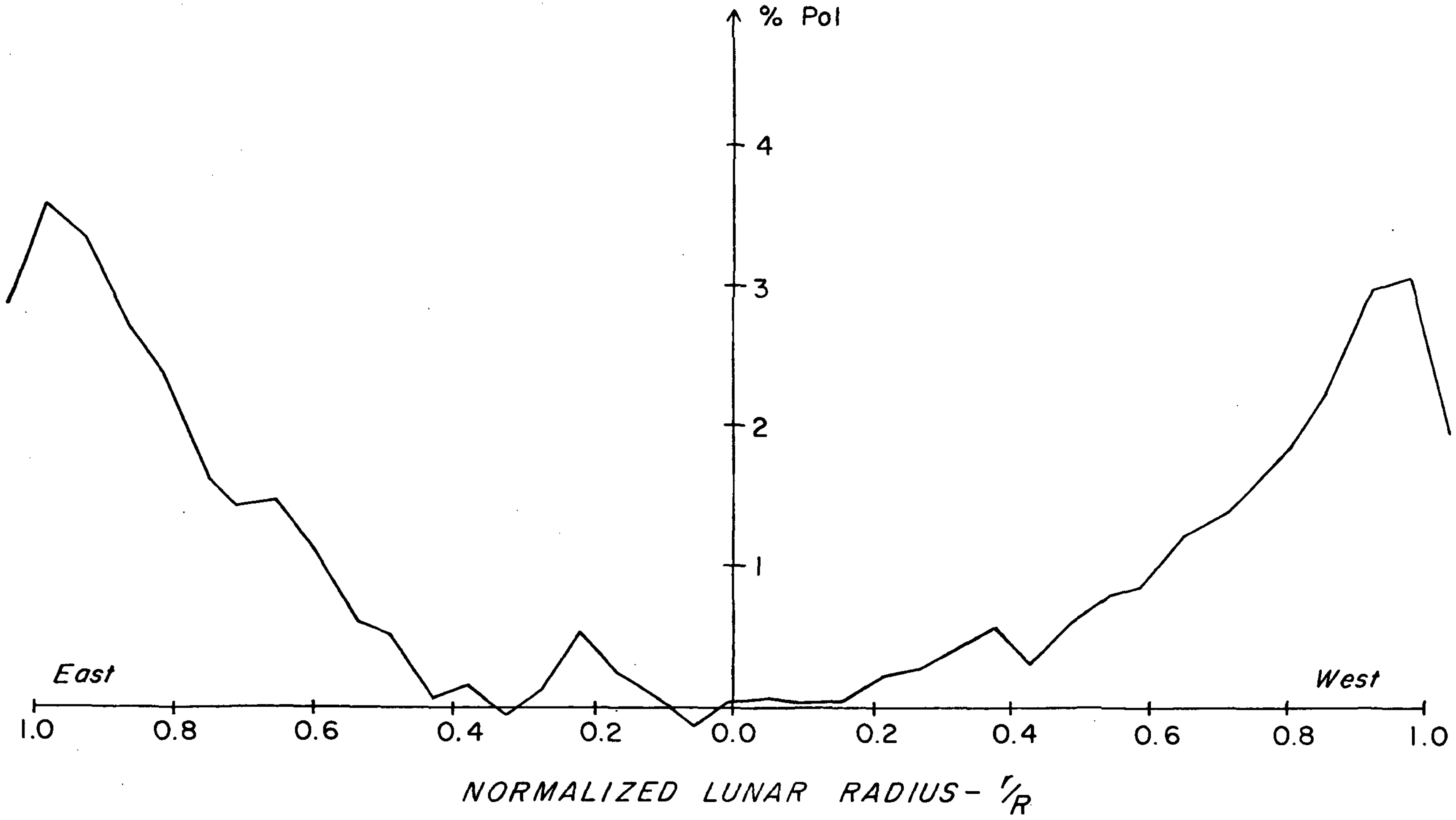

LINEAR PERCENT POLARIZATION FOR DATA SET NUMBER 2

Fig. 20

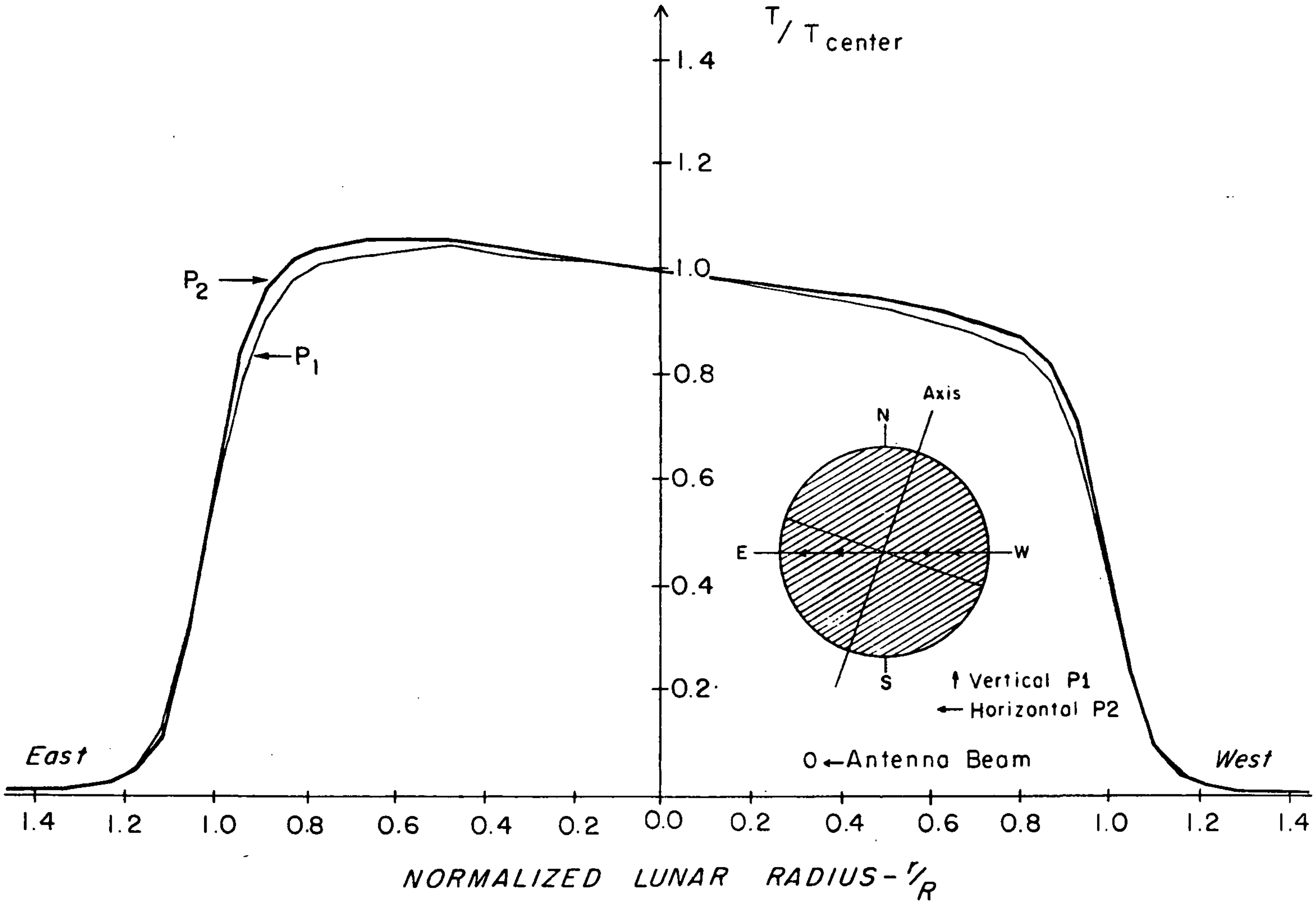

P1 AND P2 POLARIZATIONS FOR DATA SET NUMBER 3

Fig. 21

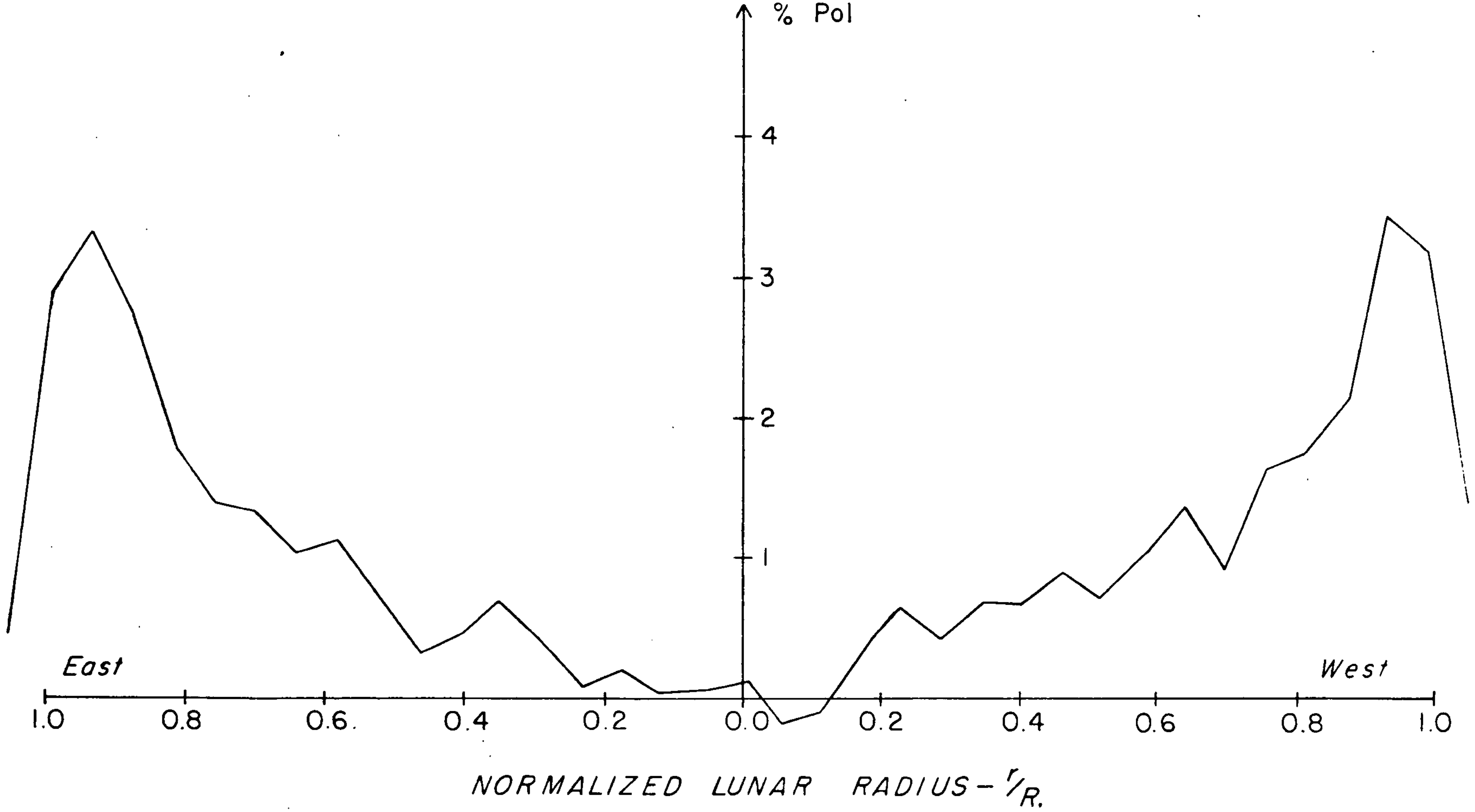

LINEAR PERCENT POLARIZATION FOR DATA SET NUMBER 3

Fig. 22

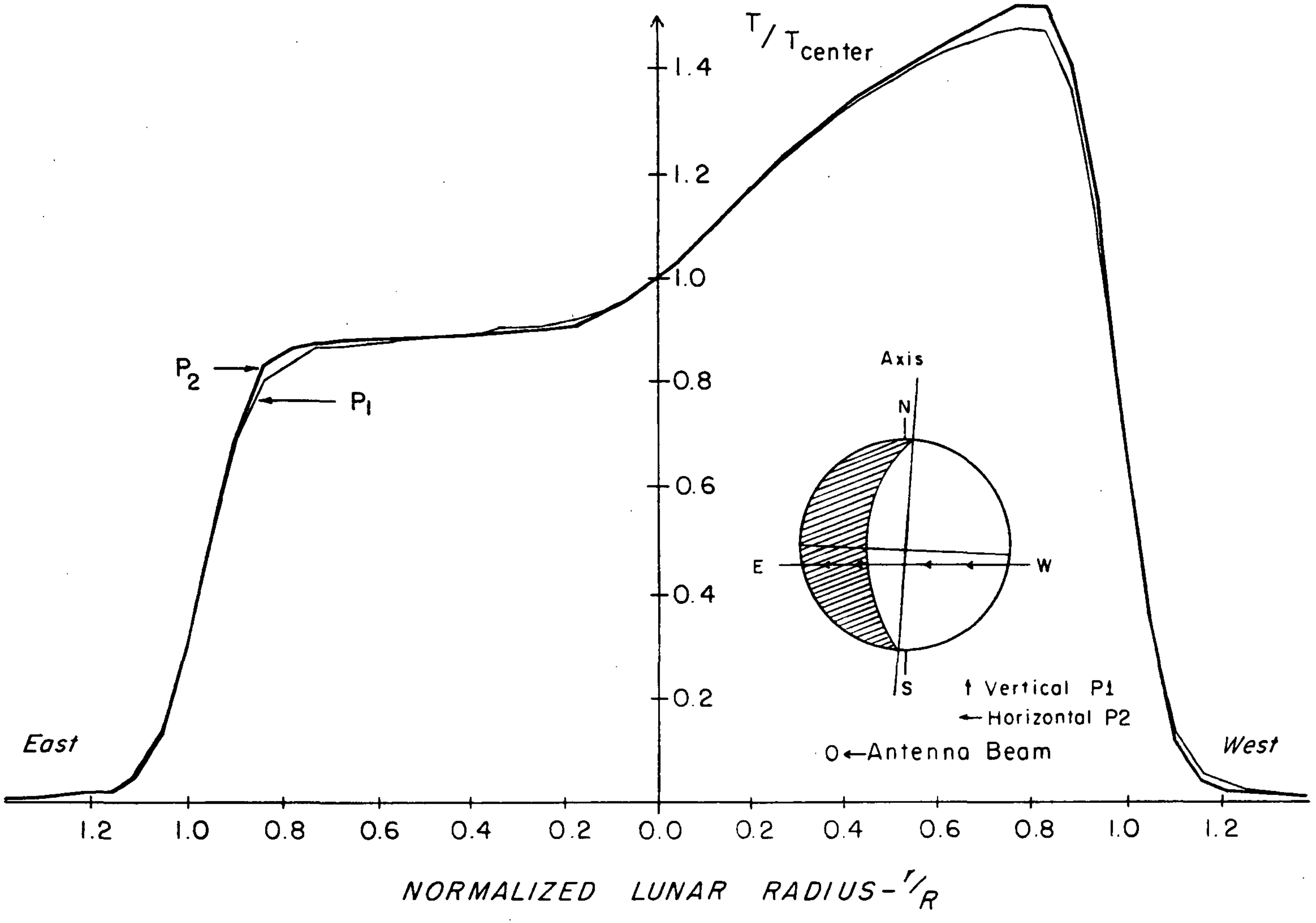

P1 AND P2 POLARIZATIONS FOR DATA SET NUMBER 4

Fig. 23

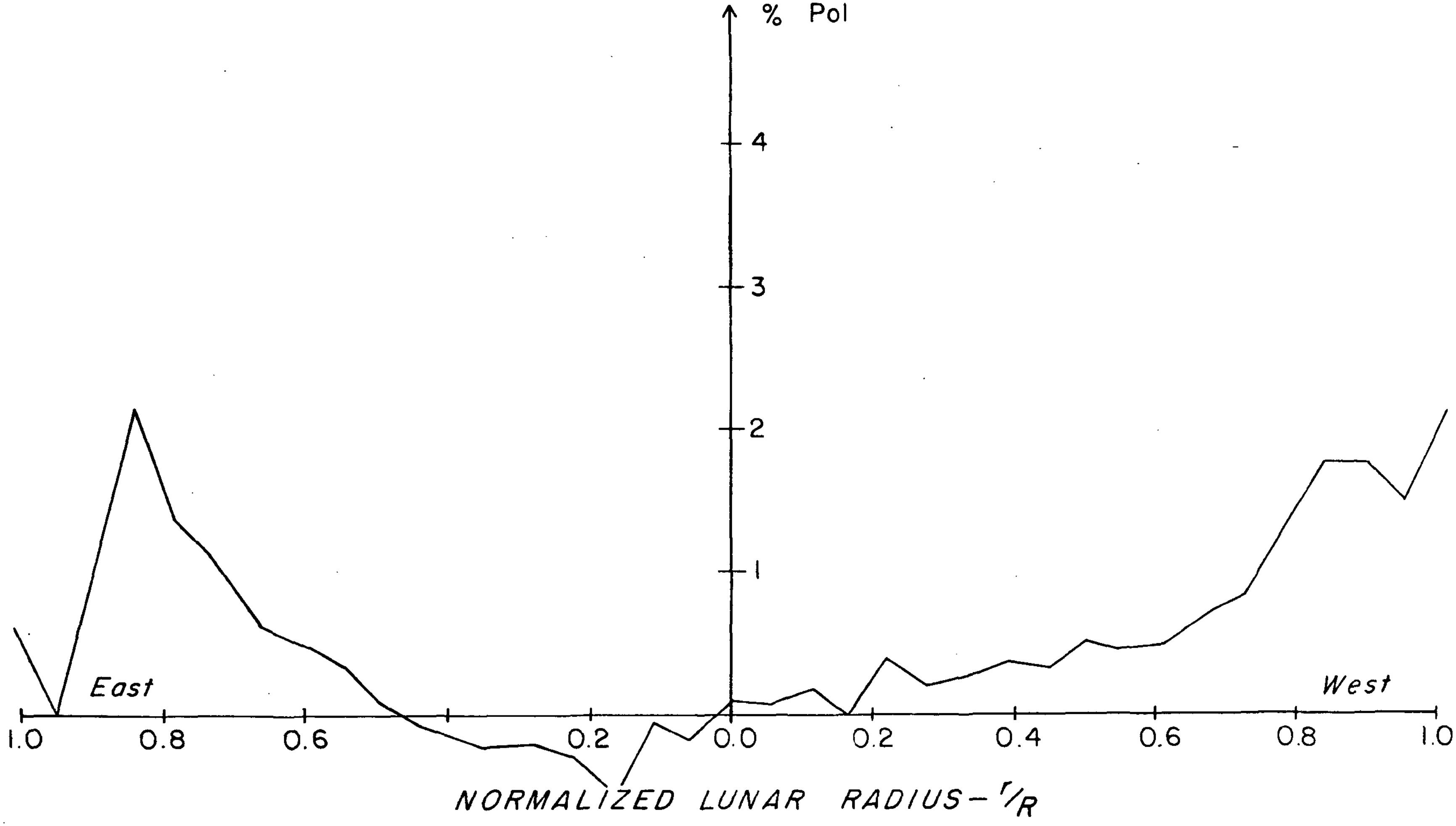

LINEAR PERCENT POLARIZATION FOR DATA SET NUMBER 4

Fig. 24

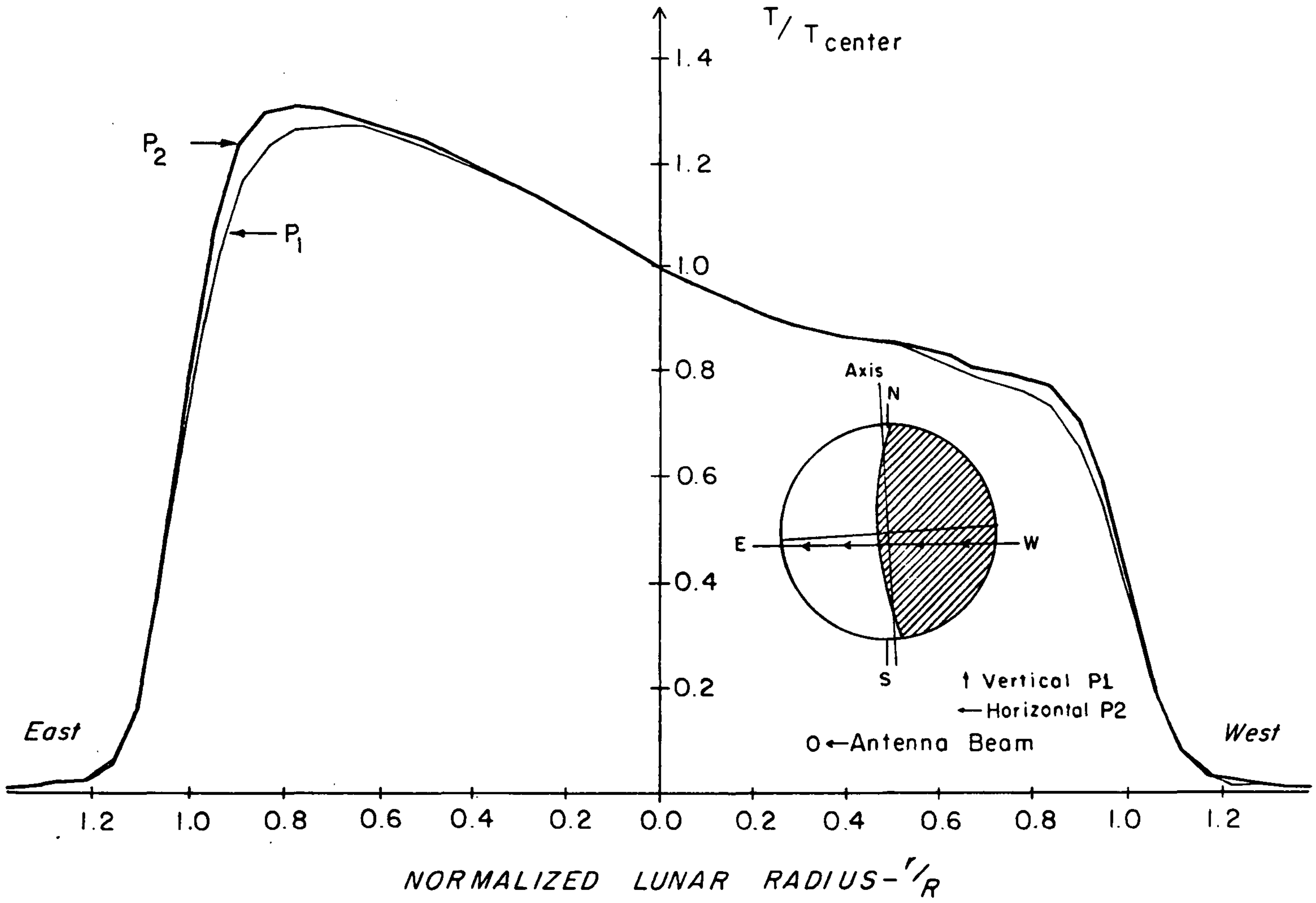

P1 AND P2 POLARIZATIONS FOR DATA SET NUMBER 5

Fig. 25

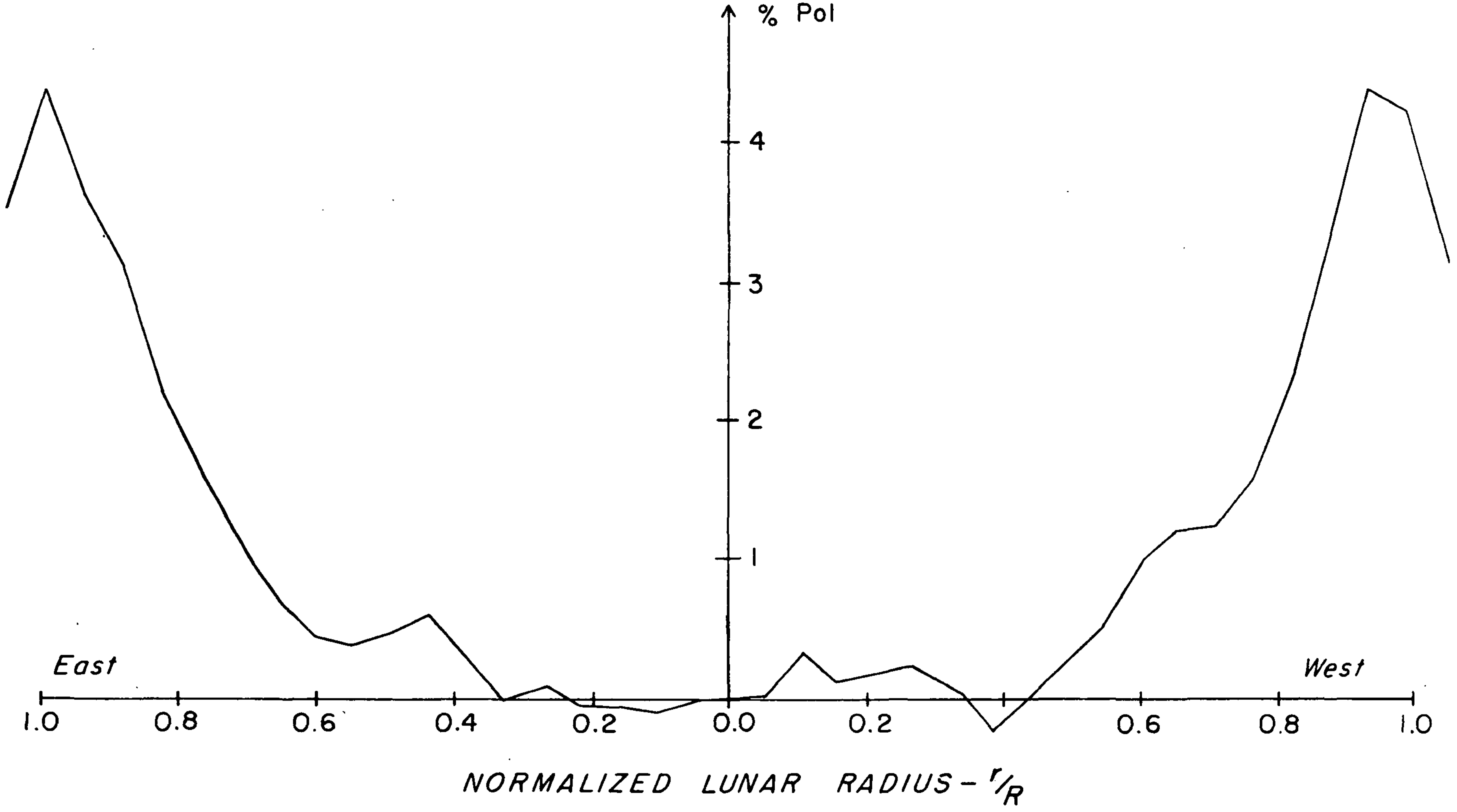

LINEAR PERCENT POLARIZATION FOR DATA SET NUMBER 5

Fig. 26

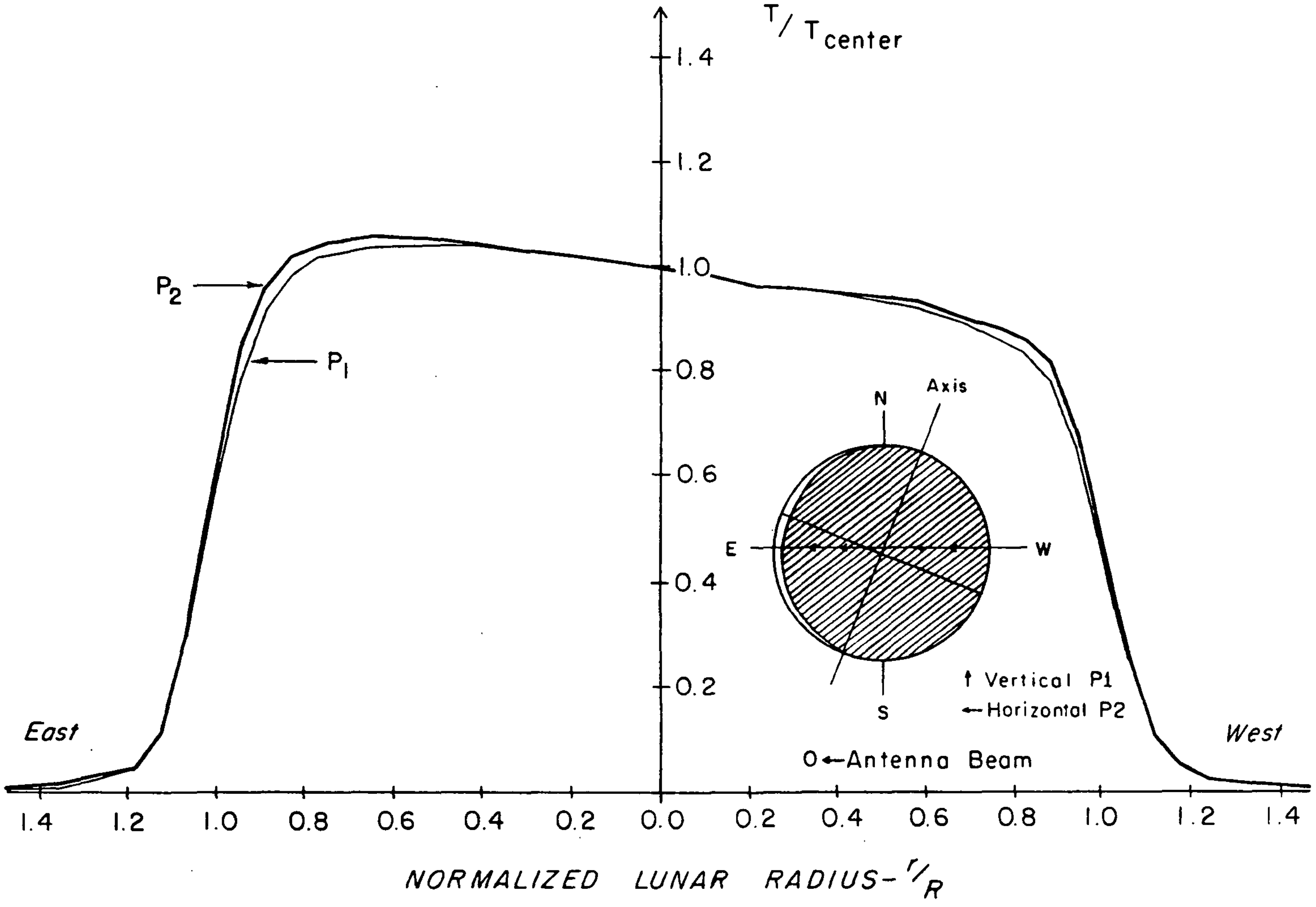

P1 AND P2 POLARIZATIONS FOR DATA SET NUMBER 6

Fig. 27

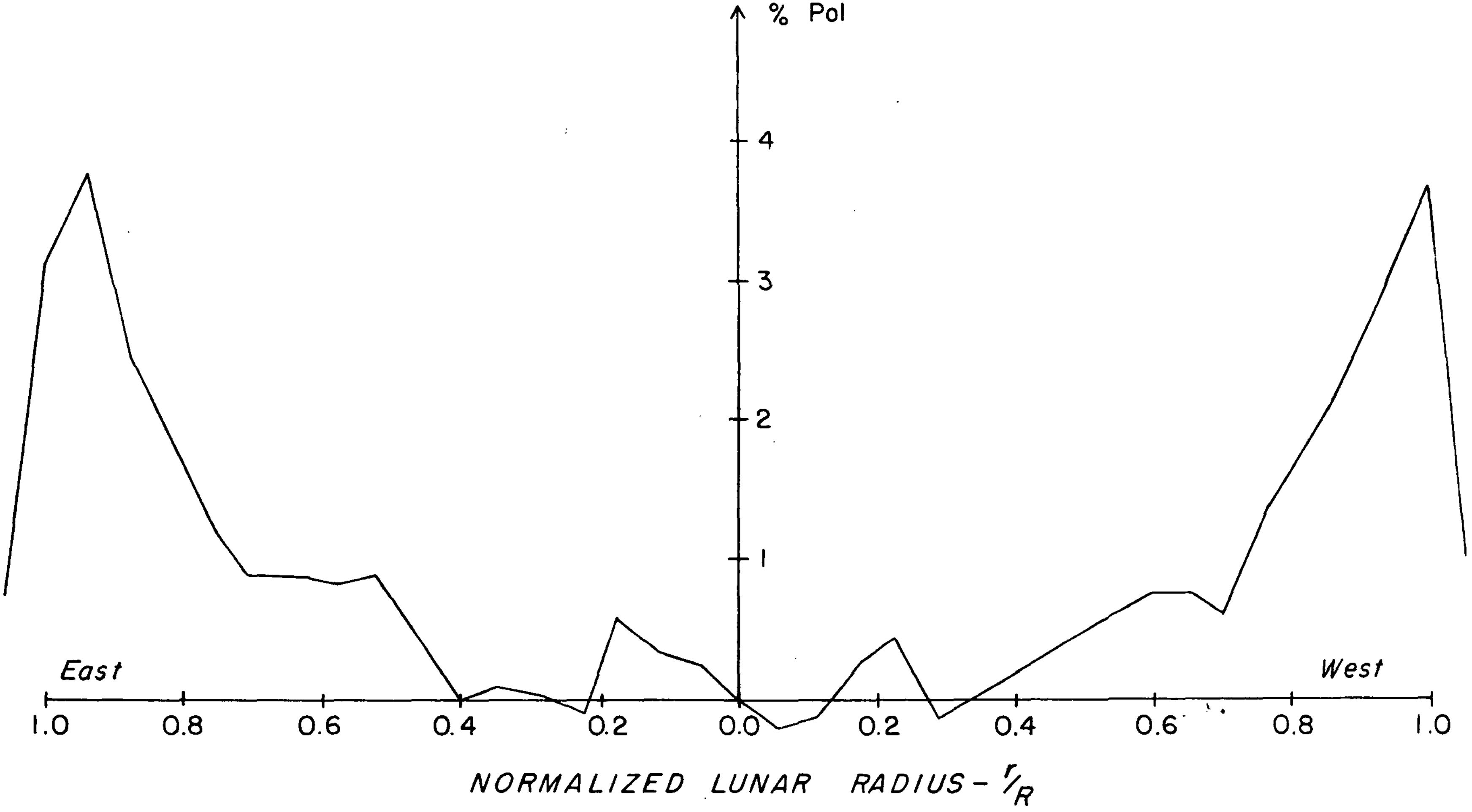

LINEAR PERCENT POLARIZATION FOR DATA SET NUMBER 6

Fig. 28

%Pol (linear percent polarization) data is roughly symmetrical about the apparent center ($r/R = 0$), as one would expect from spherical symmetry, and the peaks occur close to the limbs ($r/R = 1$). Also, the data is approximately zero at the center due to the manner in which the data is analyzed (see Chapter VII).

All six of the data sets have roughly the same magnitudes for the peaks (approximately 3-4%), except for data set number four in Fig. 24. This set is unique because the magnitudes of the peaks are only about 1.8%. This small value can be explained by comparing this data set with the curves in Fig. 14. The center offset for the fourth data set is .14, the largest of all the six data sets. This large offset is probably responsible for the low peaks.

Another unique feature of the fourth data set are the large negative values for the %Pol at $r/R = .2$, east of the center. The rough model fails to predict this sort of asymmetrical behavior for the %Pol data.

The results of the nonlinear regressions on the six data sets are summarized in Table 2. The confidence limits on ϵ and σ are based on the coupling of the two parameters in the rough model (Snedecor's F-distribution). A linearized version of the nonlinear model was used to calculate the approximate 95% confidence limits for ϵ and σ.

Initially, both model parameters were allowed to vary with the results shown as the first iteration in Table 2. From the table one can see that σ changed from data set to data set which is somewhat inconsistent for a physical parameter that should be approximately constant from one data set to the next. Therefore, a second iteration was devised setting σ equal to σ_{av}, the average of all six σ's, and letting ϵ vary. These results are shown in Table 2 as the second iteration. The final average dielectric constant for all six data sets is shown in Table 2 as 1.34±.08. The average standard deviation of slopes is 18°±2°. Confidence limits are approximately two standard deviations in the same units as the quantity.

In Fig. 29 the average dielectric constant is compared to those of previous workers in the field. The effective dielectric constant for the model (smooth or rough) which gave the best fit to the worker's data is quoted along with the appropriate error bars. Also note that four of the measurements have no error bars plotted because no errors were reported by those workers.

The models which fit the data best at long wavelengths are smooth, while the rough models give the best fit at shorter wavelengths. This would seem to indicate that the lunar surface is relatively smooth on a scale of approximately 10 cm and that roughness plays an important part in depolarizing the linearly polarized emission at wavelengths shorter than 10 cm. The depolarizing effect of roughness can readily be seen in Fig. 13.

If the high value for the effective dielectric constant obtained by Clegg and Carter, as shown in Fig. 29, is ignored, the effective dielectric constant is clearly shown to decrease with decreasing wavelength

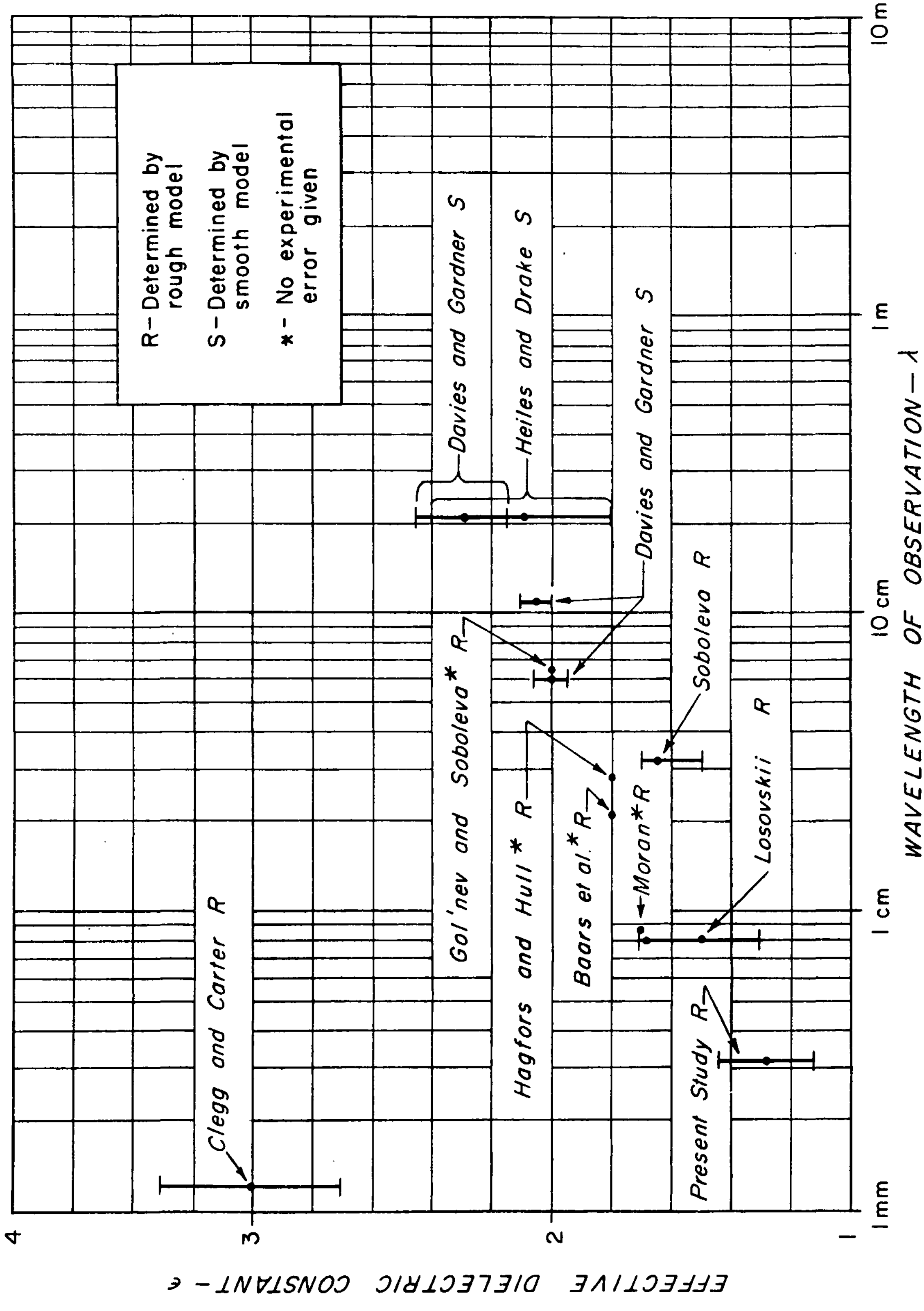

COMPARISON OF RESULTS

Fig. 29

of observation. This effect is possibly due to the inability of the rough models to adequately account for roughness on the order of a wavelength. More work needs to be done in developing models for intermediate as well as large scale surface roughness.

Another possible explanation for the decrease in the effective dielectric constant with decreasing wavelength may be that the lunar surface is layered with a dense, high dielectric constant material underlying a less dense, low dielectric constant material at the surface. Hagfors[30] has developed just such a two layered model to account for the microwave emission data and also the radar reflectivity measurements.

Before such a wavelength dependent model can be used, though, there needs to be a set of accurate lunar emission measurements taken at several wavelengths using a complete, consistent rough model with shadowing included to more carefully define the dependence of the effective dielectric constant upon wavelength.

APPENDIX A

DERIVATION OF THE BRIGHTNESS TEMPERATURE DISTRIBUTION FOR A SMOOTH DIELECTRIC SPHERE

The purpose of this Appendix is to derive an equation for the thermal emission temperature from a point on a dielectric sphere located in free space, as shown in Fig. 7.

The radius R of the sphere is much greater than the wavelength of the observed thermal emission so that the curvature of the spherical surface approaches a flat plane compared to a wavelength. The observer is normal to the page and the observer is assumed to possess infinite resolution. Also, we will require that the observer can only measure linearly polarized radiation parallel to his plane of polarization. The plane of polarization makes an arbitrary angle θ_o with a reference plane taken to be the equatorial plane of the sphere.

The angle θ is measured from the equatorial plane to the point of emission (point P). The surface normal $\vec{n}$ at point P makes an angle β_t with the observer's line-of-sight.

The plane of incidence for point P is always defined as the plane containing the surface normal $\vec{n}$ and $\vec{k}_t$, the unit vector along the observer's line-of-sight. The plane of incidence as viewed by the observer appears as a chord drown from the apparent center of the disk (point C) to the point of emission. Note that β_t is measured in the plane of incidence and therefore cannot be seen in Fig. 7.

The two electric field components of polarized emission perpendicular to $\vec{k}_t$ are shown to be $\vec{E}_{t\parallel}$ and $\vec{E}_{t\perp}$ where the "t" subscript refers to transmitted quantities. The "$\parallel$" and "$\perp$" notation refers to quantities which are parallel and perpendicular to the plane of incidence, respectively. In order to find out what the observer measures, $\vec{E}_{t\parallel}$ and $\vec{E}_{t\perp}$ are resolved along the observer's plane of polarization as

$$|\vec{E}_t| = |\vec{E}_{t\parallel}| \cos(\theta - \theta_o) - |\vec{E}_{t\perp}| \sin(\theta - \theta_o), \qquad (70)$$

where $|\vec{E}_t|$ is the magnitude of the electric field vector along the observer's plane of polarization.

The normal component of the time average energy flow per unit surface area per unit bandwidth per unit solid angle out of point P is $\langle \vec{S}_t \cdot \vec{n} \rangle$, given by the time average of the real part of the complex Poynting vector as

$$\langle \vec{S}_t \cdot n \rangle = \frac{\sqrt{\epsilon_o}}{2} \langle |\vec{E}_t|^2 \rangle \cos \beta_t, \qquad (71)$$

in watts - m^{-2} - Hz^{-1} - rad^2 where the bracket notation implies a time average. If Equation 70 is substituted into the above equation, we have

$$\langle \vec{S}_t \cdot \vec{n} \rangle = \frac{\sqrt{\epsilon_o} \cos \beta_t}{2} \Big[\langle |E_{t\parallel}|^2 \rangle \cos^2 (\theta - \theta_o)$$

$$- \langle |\vec{E}_{t\parallel}| \, |\vec{E}_{t\perp}| \rangle \sin 2(\theta - \theta_o) + \langle |\vec{E}_{t\perp}|^2 \rangle \sin^2 (\theta - \theta_o) \Big]. \qquad (72)$$

Stratton[31] defines the transmission coefficients for emitted energy parallel and perpendicular to the plane of incidence as (see Fig. 5)

$$\tau_{\parallel} \triangleq \frac{\sqrt{\epsilon_o} \cos \beta_t \langle |\vec{E}_{t\parallel}|^2 \rangle}{\sqrt{\epsilon\epsilon_o} \cos \beta_i \langle |\vec{E}_{i\parallel}|^2 \rangle}, \tag{73}$$

and

$$\tau_{\perp} \triangleq \frac{\sqrt{\epsilon_o} \cos \beta_t \langle |\vec{E}_{t\perp}|^2 \rangle}{\sqrt{\epsilon\epsilon_o} \cos \beta_i \langle |\vec{E}_{i\perp}|^2 \rangle}, \tag{74}$$

where $\vec{E}_{i\parallel}$ and $\vec{E}_{i\perp}$ are the incident electric fields parallel and perpendicualr to the plane of incidence, respectively. The angle β_i is measured from the incident wave number $\vec{k}_i$ to the surface normal $\vec{n}$. The transmission coefficients for the emitted energy are used since the emitted energy is an observable quantity.

Now we can use Equations 73 and 74 to eliminate $\vec{E}_{t\parallel}$ and $\vec{E}_{t\perp}$ from Equation 72 so that

$$\langle \vec{S}_t \cdot \vec{n} \rangle = \frac{\sqrt{\epsilon\epsilon_o} \cos \beta_i}{2} \Big[\langle |\vec{E}_{i\parallel}|^2 \rangle \tau_{\parallel} \cos^2 (\theta - \theta_o)$$

$$- \sqrt{\tau_{\parallel}\tau_{\perp}} \langle |\vec{E}_{i\parallel}| \, |\vec{E}_{i\perp}| \rangle \sin 2(\theta - \theta_o) + \langle |\vec{E}_{i\perp}|^2 \rangle \tau_{\perp} \sin^2 (\theta - \theta_o) \Big]. \tag{75}$$

Since the incident wave arises from thermal emission, the electric fields are completely unpolarized or

$$\langle |\vec{E}_{i\parallel}|^2 \rangle = \langle |\vec{E}_{i\perp}|^2 \rangle = \langle |\vec{E}_i|^2 \rangle. \tag{76}$$

Also the incident fields $\vec{E}_{i\parallel}$ and $\vec{E}_{i\perp}$ are mutually incoherent implying that

$$\langle |\vec{E}_{i\parallel}|\ |\vec{E}_{i\perp}| \rangle = 0. \tag{77}$$

Now Equation 75 becomes

$$\langle \vec{S}_t \cdot \vec{n} \rangle = \frac{\sqrt{\epsilon\epsilon_o}\ \cos\beta_i}{2} \langle |\vec{E}_i|^2 \rangle \left[\tau_\parallel \cos^2(\theta - \theta_o) + \tau_\perp \sin^2(\theta - \theta_o)\right]. \tag{78}$$

The normal component of the time averaged energy flow per unit surface area per unit bandwidth per unit solid angle inside the surface toward point P is

$$\langle \vec{S}_i \cdot \vec{n} \rangle = \frac{\sqrt{\epsilon\epsilon_o}\ \cos\beta_i}{2} \langle |\vec{E}_i|^2 \rangle, \tag{79}$$

in watts - m^{-2} - Hz^{-1} - rad^2 and now

$$\langle \vec{S}_t \cdot \vec{n} \rangle = \langle \vec{S}_i \cdot \vec{n} \rangle \left[\tau_\parallel \cos^2(\theta - \theta_o) + \tau_\perp \sin^2(\theta - \theta_o)\right]. \tag{80}$$

Since the Moon closely approximates a blackbody radiator at radio wavelengths, the Rayleigh-Jeans law gives the brightness of point P as

$$B = \frac{2kT}{\lambda^2}, \tag{81}$$

where T is the constant surface temperature in °K, k is Boltzmann's constant in joule - $k°^{-1}$, λ is the wavelength of observation in m, and B is the brightness of point P in watts - m^{-2} - Hz^{-1} - rad^{-2}.

The quantity $\langle \vec{S}_i \cdot \vec{n} \rangle$ is also referred to as the intensity of the incident subsurface radiation on point P. Provided we can neglect intervening losses in the region between the source of the thermal radiation and the surface, the intensity is equal to the brightness or

$$\langle \vec{S}_t \cdot \vec{n} \rangle = \frac{2kT}{\lambda^2}\left[\tau_{\parallel} \cos^2(\theta - \theta_o) + \tau_{\perp} \sin^2(\theta - \theta_o)\right]. \tag{82}$$

The received power per unit bandwidth for an antenna which is trained on point P is (see Chapter II)

$$w = \frac{1}{2} A_e \underset{\text{source}}{\int\int} \langle \vec{S}_t \cdot \vec{n} \rangle P_n(\theta, \varphi)\, d\Omega = kT_{\theta_o}, \tag{83}$$

where w is the received power per unit bandwidth in watts - Hz^{-1}; $P_n(\theta, \varphi)$ is the normalized power radiation pattern; A_e is the effective area of the antenna in m^2, and T_{θ_o} is the corresponding antenna temperature in °K. Now let the antenna have an infinitely narrow beamwidth so that Equation 83 becomes

$$kT_{\theta_o} = \frac{kT A_e \Omega_a}{\lambda^2}\left[\tau_{\parallel} \cos^2(\theta - \theta_o) + \tau_{\perp} \sin^2(\theta - \theta_o)\right]. \tag{84}$$

However, it can be shown that

$$A_e \Omega_a = \lambda^2, \tag{85}$$

so that Equation 84 becomes

$$T_{\theta_o} = T\left[\tau_{\parallel} \cos^2(\theta - \theta_o) + \tau_{\perp} \sin^2(\theta - \theta_o)\right]. \tag{86}$$

The difference between $T_{0°}$ and $T_{90°}$ is greatest, therefore

$$T_{0°} = T\left[\tau_{\parallel} \cos^2 \theta + \tau_{\perp} \sin^2 \theta\right], \tag{87}$$

and

$$T_{90°} = T\left[\tau_{\parallel} \sin^2 \theta + \tau_{\perp} \cos^2 \theta\right]. \tag{88}$$

Two orthogonal polarization positions are now defined for the antenna as (see Fig. 12)

$$P1 \triangleq 90°, \tag{89}$$

and

$$P2 \triangleq 0°. \tag{90}$$

Equations 87 and 88 now become

$$T_{P1} = T\left[\tau_{\parallel} \sin^2 \theta + \tau_{\perp} \cos^2 \theta\right], \tag{91}$$

and

$$T_{P2} = T\left[\tau_{\parallel} \cos^2 \theta + \tau_{\perp} \sin^2 \theta\right]. \tag{92}$$

For clarity, Equations 91 and 92 can be expressed as functions of ϵ, β_t, and θ so that (dropping the t subscript on β)

$$T_{P1}(\epsilon, \beta, \theta) = T\left[\tau_{\parallel}(\epsilon, \beta) \sin^2 \theta + \tau_{\perp}(\epsilon, \beta) \cos^2 \theta\right], \tag{93}$$

and

$$T_{P2}(\epsilon, \beta, \theta) = T\left[\tau_{\parallel}(\epsilon, \beta) \cos^2 \theta + \tau_{\perp}(\epsilon, \beta) \sin^2 \theta\right]. \tag{94}$$

The above equations now represent the true brightness temperature for a point at temperature T, located by the angles β and θ on a dielectric sphere with a dielectric constant of ϵ.

APPENDIX B

ONE ADVANTAGE OF DISPLAYING DATA AS A LINEAR PERCENT POLARIZATION

The purpose of this Appendix is to show that displaying the lunar emission data as a percent of the total polarization, rather than as a simple difference of polarizations, achieves a higher signal-to-noise ratio by effectively decreasing the amount of noise present in the data.

The final polarization signals (after averaging to reduce receiver noise) for the vertical and horizontal polarizations are $S_{P1}(x_i)$ and $S_{P2}(x_i)$, respectively, where

$$S_{P1}(x_i) \triangleq T_{aP1}(x_i) + n_1(x_i), \tag{95}$$

and

$$S_{P2}(x_i) \triangleq T_{aP2}(x_i) + n_2(x_i). \tag{96}$$

The noise free polarization signals for the Moon are given by $T_{aP1}(x_i)$ and $T_{aP2}(x_i)$ (previously derived and written as Equations 61 and 62 in Chapter V). The receiver noise, model errors and other sources of error in both the vertical and horizontal polarizations are represented by $n_1(x_i)$ and $n_2(x_i)$, respectively. The independent variable x_i represents the i^{th} data point in the time or angular domain and conversion between the two domains is accomplished by knowing the velocity of the Moon with respect to the antenna beam.

The mean and variance of $n_1(x_i)$ and $n_2(x_i)$ are

$$\langle n_i(x_i)\rangle = \langle n_2(x_i)\rangle = 0, \qquad (97)$$

and

$$\langle n_1(x_i)^2\rangle = \sigma_1^{\,2}; \qquad (98)$$

$$\langle n_2(x_i)^2\rangle = \sigma_2^{\,2}. \qquad (99)$$

where the bracket notation implies a finite time average with $\sigma_1^{\,2}$ and $\sigma_2^{\,2}$ being unknown quantities. Also $n_1(x_i)$ and $n_2(x_i)$ are assumed to be jointly normal random variables that are uncorrelated with each other or

$$\langle n_1(x_i)\, n_2(x_i)\rangle = 0. \qquad (100)$$

This assumption of normality is not unreasonable in most cases since there is a tendency for $n_1(x_i)$ or $n_2(x_i)$, a total error due to the sum of many individual sources of error, to be normally distributed because of the Central Limit Theorem.

Suppose we wish to display the lunar data as a difference of two orthogonal polarizations given by $\Delta S(x_i)$ as

$$\Delta S(x_i) \mathrel{\hat{=}} S_{P2}(x_i) - S_{P1}(x_i), \qquad (101)$$

or

$$\Delta S(x_i) = T_{aP2}(x_i) - T_{aP1}(x_i) + n_2(x_i) - n_1(x_i). \qquad (102)$$

The postulated model is given by $\Delta T(x_i)$ as

$$\Delta T(x_i) \mathrel{\hat{=}} T_{aP2}(x_i) - T_{aP1}(x_i). \qquad (103)$$

Equation 102 now becomes

$$\Delta S(x_i) = \Delta T(x_i) + n_2(x_i) - n_1(x_i). \qquad (104)$$

Now if the postulated model is least squares fitted to the data and if the postulated model is the true model, then S^2, the residual mean square, is

$$S^2 = \frac{\sum_{i=1}^{n} \left[\Delta S(x_i) - \Delta T(x_i)\right]^2}{n - 2}, \qquad (105)$$

which further simplifies to

$$S^2 = \frac{\sum_{i=1}^{n} \left[n_2(x_i) - n_1(x_i)\right]^2}{n - 2}. \qquad (106)$$

The factor of n - 2 in the denominator comes from the fact that there are n data points with 2 model parameters to be determined from the regression or n - 2 degrees of freedom.

If n is large then the sum in Equation 106 approaches a time average or

$$S^2 = \frac{\sum_{i=1}^{n} \left[n_2(x_i) - n_1(x_i)\right]^2}{n - 2} = \langle [n_2(x_i) - n_1(x_i)]^2 \rangle, \qquad (107)$$

and Equations 97 and 100 can be used to simplify Equation 107 to read

$$S^2 = \langle n_1{}^2(x_i) + n_2{}^2(x_i) \rangle = \sigma_1{}^2 + \sigma_2{}^2 . \qquad (108)$$

In practice, the difference of two polarizations, $\Delta T(x_i)$ is folded about the center of the lunar disk and averaged because the model exhibits symmetry about the lunar center. Such a process has been done by Moran[32], and others.[33, 34] The effect of folding and averaging is to reduce the residual mean squares by a factor of 2 so that

$$S_{fold}^{2} = \frac{\sigma_1^2 + \sigma_2^2}{2} . \tag{109}$$

The standard deviation of the residual is obtained by taking the square root of residual mean squares or

$$S_{fold} = \sqrt{\frac{\sigma_1^2 + \sigma_2^2}{2}} . \tag{110}$$

Also if $\sigma_1 = \sigma_2 = \sigma'$ then S_{fold} becomes

$$S_{fold} = \sigma' . \tag{111}$$

This result will be used later for comparison with a new method for displaying the lunar data as a true percent of the total polarization signal.

First, the average polarization signal will be defined as

$$T_{av}(x_i) \triangleq \frac{T_{aP1}(x_i) + T_{aP2}(x_i)}{2} , \tag{112}$$

and the percent polarization is taken to be

$$\%Pol_s(x_i) \triangleq \frac{S_{P2}(x_i) - S_{P1}(x_i)}{S_{P1}(x_i) + S_{P2}(x_i)} . \tag{113}$$

Equations 95, 96, 103, and 112 may be substituted into the above expression which simplifies as

$$\%\mathrm{Pol}_s(x_i) = \frac{\Delta T(x_i) + n_2(x_i) - n_1(x_i)}{2\,T_{av}(x_i) + n_1(x_i) + n_2(x_i)} \quad . \tag{114}$$

If the signals have a sufficiently high signal-to-noise ratio, then the condition that

$$2T_{av}(x_i) >> n_1(x_i) + n_2(x_i), \tag{115}$$

is satisfied for all x_i on or near the lunar disk. This condition will not be satisfied away from the disk of the Moon since the noise would dominate over the Moon's signal. We are, however, only interested in the data across the lunar disk so that Equation 115 is always satisfied and Equation 114 becomes

$$\%\mathrm{Pol}_s(x_i) = \frac{\Delta T(x_i) + n_2(x_i) - n_1(x_i)}{2T_{av}(x_i)} \, . \tag{116}$$

The postulated model is defined as

$$\%\mathrm{Pol}_T(x_i) \triangleq \frac{\Delta T(x_i)}{2T_{av}(x_i)} \, , \tag{117}$$

and the residual mean square due to the least squares regression of the model to the data is

$$S_{\%}^{\;2} = \frac{\sum\limits_{i=1}^{n} \left[\%\mathrm{Pol}_s(x_i) - \%\mathrm{Pol}_T(x_i)\right]^2}{n - 2} \, . \tag{118}$$

Using Equations 116 and 117 to simplify the above expression we have

$$S_{\%}^2 = \frac{\sum_{i=1}^{n} \left[\frac{n_2(x_i) - n_1(x_i)}{2\,T_{av}(x_i)}\right]^2}{n-2} . \tag{119}$$

If n is large then the above summation approaches a time average and

$$S_{\%}^2 = \left\langle \left[\frac{n_2(x_i) - n_1(x_i)}{2T_{av}(x_i)}\right]^2 \right\rangle . \tag{120}$$

The squared term in the bracket may be expanded and simplified by using Equation 100 so that

$$S_{\%}^2 = \frac{1}{4} \left\langle \frac{n_1^{\,2}(x_i) + n_2(x_i)}{T_{av}^{\,2}(x_i)} \right\rangle . \tag{121}$$

In order to evaluate the above equation further, we must make certain assumptions about $T_{av}(x_i)$, the average polarization signal. The lunar polarization data in Figs. 17, 19, 21, 23, 25, and 27 can be approximated for .8 of a lunar radius on either side of the apparent center by a simple linearly varying function, or

$$T_{av}(x_i) = mx_i + 1, \quad (-.8 \leq x_i \leq .8), \tag{122}$$

where m is the slope of the observed temperature distribution and x_i is now measured in units of a normalized lunar radius. Also note that the ordinates have been normalized to unity at the apparent center. Equation 121 now becomes

$$S_{\%}^2 = \frac{1}{4} \left\langle \frac{n_1^2(x_i) + n_2^2(x_i)}{(mx_i + 1)^2} \right\rangle . \tag{123}$$

If we replace the time average brackets by its integral representation then

$$S_{\%}^2 = \frac{1}{4} \cdot \frac{1}{2(.8)} \int_{-8}^{.8} \frac{n_1^2(x_i) + n_2^2(x_i)}{(mx_i + 1)^2} \, dx_i , \tag{124}$$

where the finite time average is carried out for 80% of the lunar diameter. Evaluation of Equation 124 is accomplished by noting that $n_1^2(x_i)$ and $n_2^2(x_i)$ are random variables that can be replaced by their variances and taken outside of the integral and

$$S_{\%}^2 = \frac{\sigma_1^2 + \sigma_2^2}{4(1 - .64m^2)} . \tag{125}$$

Note here that the slope never exceeds ±.4 for all the data sets obtained so that a worst case for the residual mean squares would be

$$S_{\%}^2 = \frac{\sigma_1^2 + \sigma_2^2}{3.5904} , \tag{126}$$

and the standard deviation is

$$S_{\%} = \sqrt{\frac{\sigma_1^2 + \sigma_2^2}{3.5904}} . \tag{127}$$

Comparing the above expression with Equation 100 we see that

$$S_{\%} = .745\ S_{\text{fold}} \tag{128}$$

for $-.8 \leq x_i \leq .8$ and for $m = \pm .4$ (worst case).

Displaying the lunar polarization data as a percent polarization now achieves a smaller standard deivation of the residuals as opposed to the folded difference of polarizations for the conditions stated herein.

REFERENCES

1. Troitskii, V. S., "Theory of Lunar Radio Emission," Astron. Zh., Vol. 31, No. 6, 1954, pp. 511-528.

2. Soboleva, N. S., "Measurement of the Polarization of Lunar Radio Emission on a Wavelength of 3.2 cm," Soviet Ast., Vol. 6, No. 6, May-June 1963, pp. 873-875.

3. Baars, J. W. M., P. G. Mezger, N. Savin and H. Wendker, "The Polarization of the Thermal Radiation of the Moon at 14.5 GHz," Astr. J., Vol. 70, No. 2, March 1965, p. 132.

4. Heiles, C. E. and F. D. Drake, "The Polarization and Intensity of Thermal Radiation from a Planetary Surface," Icarus, Vol. 2, 1963, pp. 281-292.

5. Golnev, V. Ya. and N. S. Soboleva, "Polarization Observations of Lunar Radio Emission," Proc. Astr. Obs. Pulkova, Vol. 13, 1964, pp. 83-88.

6. Moran, J. M., Jr., "Radiometric Observations of the Moon Near 1 cm Wavelength," M.S. Thesis, M.I.T., Cambridge, Mass., 1965.

7. Hagfors, T. and Moriello, J., "The Effect of Roughness on the Polarization of Thermal Emission from a Surface," J. Res. NBS, Vol. 69D, Radio Sci., 1965, pp. 1614-1615.

8. Hagfors, T., "Remote Probing of the Moon by Infrared and Microwave Emissions and by Radar," Radio Science, Vol. 5, No. 2, Feb. 1970, pp. 189-227.

9. Losovskii, B. Ya., "Observations of Polarization of Lunar Radio Emission at 0.8 cm with High Resolution," Astron. Zh., Vol. 11, No. 2, Sept.-Oct. 1967, pp. 329-331.

10. Lynn, V. L., M. D. Sohigian and E. A. Crocker, "Radar Observations of the Moon at a Wavelength of 8.6 Millimeters," J. Geophys. Res., Vol. 69, No. 4, Feb. 1964, pp. 781-783.

11. Davies, R. D. and F. F. Gardner, "Linear Polarization of the Moon at 6, 11, and 21 cm Wavelengths," Aust. J. Phys., Vol. 19, 1966, pp. 823-836.

12. Clegg, P. E. and B. S. Carter, "Measurements of Lunar Radiation in the Wavelength Range Centered at 1.2 mm," Mon. Not. R. Astr. Soc., Vol. 148, 1970, pp. 261-274.

13. Straiton, A. W. and B. M. Fannin, "Comparison of 15 GHz Propagation Data from the ATS-5 Satellite with Ground Based Radio and Meteorological Data," Proceedings of the XVI Symposium on EEP/AGARD, Sept. 1970, Dusseldorf, Germany, pp. 10-1 to 10-9.

14. Stratton, J. A., Electromagnetic Theory, McGraw-Hill Book Co., New York, 1941, p. 496.

15. Clegg, P. E. and B. S. Carter, op. cit., ref. 12, p. 271.

16. Williamson, J. B. P., J. Pullen and R. T. Hunt, "The Shape of Solid Surfaces," Surface Mechanics: ASME Winter Annual Meeting, Los Angeles, California, Nov. 1969, pp. 16-21.

17. Beckmann, P. and A. Spizzichino, The Scattering of Electromagnetic Waves from Rough Surfaces, Pergamon Press, New York, 1963, pp. 193-194.

18. Smith. B. G., "Lunar Surface Roughness: Shadowing and Thermal Emission," J. Geophys. Res., Vol. 72, No. 16, August 1967, pp. 4059-4067.

19. Brockelman, R. A. and T. Hagfors, "Note on the Effect of Shadowing on the Backscattering of Waves from a Random Rough Surface," T-AP, Vol. AP-14, No. 5, Sept. 1966, pp. 621-629.

20. "Dielectric Properties of Basalt Powders," National Aeronautics and Space Administration, George C. Marshall Space Flight Center, Arthur D. Little, Inc. Report No. 71679, June 1970.

21. Cogdell, J. R., "Calibration Program for the 16-Foot Antenna," Technical Report No. NGL-006-69-1, Electrical Engineering Research Laboratory, The University of Texas at Austin, Jan. 1969, pp. 6-9.

22. Tolbert, C. W., A. W. Straiton, and L. C. Krause, "A 16-Foot Diameter Millimeter Wavelength Antenna System, Its Characteristics and Applications," T-AP, Vol. AP-13, No. 2, March 1965, pp. 225-229.

23. Davis, J. H., and J. R. Cogdell, "Pointing of the 16-Foot Antenna," Technical Memorandum No. NGL-006-69-3, Electrical Engineering Research Laboratory, The University of Texas at Austin, Nov. 1969.

24. Davis, J. H., "The Evaluation of Reflector Antennas," Technical Report No. NGL-006-70-1, Electrical Engineering Research Laboratory, The University of Texas at Austin, May 1970, pp. 98-123.

25. Cogdell, J. R., J. J. G. McCue, P. D. Kalachev, A. E. Salomonovich, I. G. Moiseev, J. M. Stacey, E. E. Epstein, E. E. Altshuler, G. Feix, J. W. B. Day, H. Hvatum, W. J. Welch, and F. T. Barath, "High Resolution Millimeter Reflector Antennas," T-AP, Vol. AP-18, No. 4, July 1970, pp. 515-529.

26. The American Ephemeris and Nautical Almanac - 1971, U. S. Government Printing Office, Washington, 1969, pp. 310-311.

27. Marquardt, D. W., "An Algorithm for Least-Squares Estimation of Nonlinear Parameters," J. Soc. Ind. Appl. Math., Vol. 2, 1963, pp. 431-441.

28. Draper, N. R. and H. Smith, Applied Regression Analysis, John Wiley and Sons, Inc., New York, 1966, pp. 263-304.

29. Marquardt, D. W. and R. M. Stanley, "NLIN2-Least Squares Estimation of Nonlinear Parameters, Supplement to S. D. A. 3093 (NLIN)," Mimeo manuscript available from the authors.

30. Hagfors, T., op. cit., ref. 8, pp. 207-217.

31. Stratton, J. W., op. cit., ref. 14, p. 496.

32. Moran, J. M., Jr., op. cit., ref. 6, p. 50.

33. Losovskii, B. Ya., op. cit., ref. 9, p. 329.

34. Davies, R. D. and F. F. Gardner, op. cit., ref. 11, p. 829.